Published in final edited form as:

Neurobiol Dis. 2021 January ; 147: 105141. doi:10.1016/j.nbd.2020.105141.

Epilepsy and neurobehavioral abnormalities in mice with a dominant-negative *KCNB1* pathogenic variant

Nicole A. Hawkins[a,1], **Sunita N Misra**[b,c,1], **Manuel Jurado**[a], **Seok Kyu Kang**[a], **Nicholas C. Vierra**[d,e], **Kimberly Nguyen**[d], **Lisa Wren**[a], **Alfred L. George Jr.**[a], **James S. Trimmer**[d,e], **Jennifer A. Kearney**[a,*]

[a]Department of Pharmacology, Northwestern University Feinberg School of Medicine, Chicago, IL 60611, United States of America

[b]Department of Pediatrics, Northwestern University Feinberg School of Medicine, Chicago, IL 60611, United States of America

[c]Ann & Robert H. Lurie Children's Hospital of Chicago Chicago, IL 60611, United States of America

[d]Department of Neurobiology, Physiology and Behavior, University of California, Davis, CA 95616, United States of America

[e]Department of preceding Physiology and Membrane Biology, University of California, Davis, CA 95616, United States of America

Abstract

Developmental and epileptic encephalopathies (DEE) are a group of severe epilepsies that usually present with intractable seizures, developmental delay, and often have elevated risk for premature mortality. Numerous genes have been identified as a monogenic cause of DEE, including *KCNB1*. The voltage-gated potassium channel $K_v2.1$, encoded by *KCNB1*, is primarily responsible for delayed rectifier potassium currents that are important regulators of excitability in electrically excitable cells, including neurons. In addition to its canonical role as a voltage-gated potassium conductance, $K_v2.1$ also serves a highly conserved structural function organizing endoplasmic reticulum-plasma membrane junctions clustered in the soma and proximal dendrites of neurons. The de novo pathogenic variant *KCNB1*-p.G379R was identified in an infant with epileptic spasms, and atonic, focal and tonic-clonic seizures that were refractory to treatment with standard antiepileptic drugs. Previous work demonstrated deficits in potassium conductance, but did not assess non-conducting functions. To determine if the G379R variant affected $K_v2.1$ clustering at endoplasmic reticulum-plasma membrane junctions, $K_v2.1$-G379R was expressed in HEK293T cells. $K_v2.1$-G379R expression did not induce formation of endoplasmic reticulum-plasma

*Corresponding author at: Department of Pharmacology, Searle 8-510, 320 East Superior St., Chicago, IL 60611, United States of America. jennifer.kearney@northwestern.edu (J.A. Kearney).

[1]Denotes equal contribution.

Supplementary data to this article can be found online at https://doi.org/10.1016/j.nbd.2020.105141.

Declaration of Competing Interest

None.

membrane junctions, and co-expression of K_v2.1-G379R with K_v2.1-wild-type lowered induction of these structures relative to K_v2.1-WT alone, consistent with a dominant negative effect. To model this variant in vivo, we introduced *Kcnb1*^{G379R} into mice using CRISPR/Cas9 genome editing. We characterized neuronal expression, neurological and neurobehavioral phenotypes of *Kcnb1*$^{G379R/+}$ (*Kcnb1*$^{R/+}$) and *Kcnb1*$^{G379R/G379R}$ (*Kcnb1*$^{R/R}$) mice. Immunohistochemistry studies on brains from *Kcnb1*$^{+/+}$, *Kcnb1*$^{R/+}$ and *Kcnb1*$^{R/R}$ mice revealed genotype-dependent differences in the expression levels of K_v2.1 protein, as well as associated K_v2.2 and AMIGO-1 proteins. *Kcnb1*$^{R/+}$ and *Kcnb1*$^{R/R}$ mice displayed profound hyperactivity, repetitive behaviors, impulsivity and reduced anxiety. Spontaneous seizures were observed in *Kcnb1*$^{R/R}$ mice, as well as seizures induced by exposure to novel environments and/ or handling. Both *Kcnb1*$^{R/+}$ and *Kcnb1*$^{R/R}$ mutants were more susceptible to proconvulsant-induced seizures. In addition, both *Kcnb1*$^{R/+}$ and *Kcnb1*$^{R/R}$ mice exhibited abnormal interictal EEG activity, including isolated spike and slow waves. Overall, the *Kcnb1*^{G379R} mice recapitulate many features observed in individuals with DEE due to pathogenic variants in *KCNB1*. This new mouse model of *KCNB1*-associated DEE will be valuable for improving the understanding of the underlying pathophysiology and will provide a valuable tool for the development of therapies to treat this pharmacoresistant DEE.

Keywords

Epilepsy; Encephalopathy; Autism spectrum disorder; Developmental disorder; Voltage-gated potassium channels; Voltage-gated ion channels; K_v2.1

1. Introduction

Developmental and epileptic encephalopathies (DEE) are a group of severe disorders that present early in life and are characterized by paroxysmal activity on EEG, multiple seizure types that are often medically intractable, and serious cognitive, behavioral and neurological deficits (Berg et al., 2010; Scheffer et al., 2017). In 30–50% of infants diagnosed with an epileptic encephalopathy, a causative mutation has been identified in a known epilepsy gene (McTague et al., 2016). Previous work has identified heterozygous de novo *KCNB1* pathogenic variants in individuals with DEE (Torkamani et al., 2014; Saitsu et al., 2015; Thiffault et al., 2015; Allen et al., 2016; Calhoun et al., 2017; de Kovel et al., 2017; Latypova et al., 2017; Marini et al., 2017; Miao et al., 2017; Bar, 2020; Kang et al., 2019). In addition to seizures, individuals with *KCNB1* variants display comorbidities that include developmental delay, intellectual disability, features of autism spectrum disorder, ADHD and aggression, as well as borderline long QT syndrome in some cases (Calhoun et al., 2017; de Kovel et al., 2017; Marini et al., 2017; Bar, 2020). Since the initial reports of *KCNB1* variants in DEE type 26 (DEE26), the phenotype has expanded to include cases with less severe and/or later onset epilepsy or no discrete seizures, and thus the term *KCNB1* encephalopathy encompasses this broader phenotype spectrum.

The *KCNB1*-p.G379R variant was identified in a male child with seizures commencing at 8 months of age (Torkamani et al., 2014). Glycine 379 is located in the K_v2.1 channel ion selectivity filter and is an evolutionarily invariant residue critical for potassium selectivity, supporting pathogenicity of the G379R missense variant (Fig. 1A) (Kuang et al., 2015). The

epilepsy phenotype included infantile spasms, atonic, focal, and tonic-clonic seizures that were refractory to various antiepileptic therapies, including topiramate, valproic acid, pyridoxine, ACTH, and the ketogenic diet (Torkamani et al., 2014). At 15 months of age, hypsarrhythmia was present on EEG and later in childhood, monitoring revealed multifocal and diffuse polyspikes, polyspike and slow waves, and diffuse polyspike bursts (Torkamani et al., 2014). The individual also had severe motor and language delays, autism spectrum disorder, and strabismus (Torkamani et al., 2014; de Kovel et al., 2017; Srivastava et al., 2018).

KCNB1 encodes the $K_V2.1$ voltage-gated potassium channel subunit that is primarily responsible for delayed rectifier potassium current, an important regulator of neuronal excitability (Murakoshi and Trimmer, 1999; Guan et al., 2007; Liu and Bean, 2014; Honigsperger et al., 2017; Palacio et al., 2017). $K_V2.1$ is widely and robustly expressed throughout the nervous system. Within neurons, the majority of $K_V2.1$ is localized to high-density clusters on the soma, proximal dendrites and axon initial segment (Trimmer, 1991; Du et al., 1998; Sarmiere et al., 2008; Bishop et al., 2015). $K_V2.1$ clusters align with and are components of endoplasmic reticulum (ER) and plasma membrane (PM) junctions (ER-PM junctions), membrane microdomains important in calcium and lipid signaling and homeostasis (Du et al., 1998; Mandikian et al., 2014; Bishop et al., 2015; Henne et al., 2015; Gallo et al., 2016; Dickson, 2017; Wu et al., 2017; Bishop et al., 2018). $K_V2.1$ serves a structural role at ER-PM junctions independent of its potassium conducting function by binding to the ER proteins VAPA and VAPB, resulting in the recruitment of the ER to the PM (Fox et al., 2015; Johnson et al., 2018; Kirmiz et al., 2018). At these sites in brain neurons, $K_V2.1$ facilitates the spatial coupling of PM L-type calcium channels with ryanodine receptor ER calcium release channels, forming compartmentalized calcium signaling microdomains (Vierra et al., 2019). In addition to neuronal expression, $K_V2.1$ is also expressed in rodent heart within high-density clusters in atrial myocytes, as well as non-clustered $K_V2.1$ in ventricular transverse-axial tubules and sarcolemma (O'Connell et al., 2008), and in high density clusters on pancreatic β cells (Fu et al., 2017).

Several *KCNB1* variants have been functionally characterized in vitro and shown to exhibit reduced $K_V2.1$ conductance, as well as altered ion selectivity, expression and localization (Torkamani et al., 2014; Saitsu et al., 2015; Thiffault et al., 2015; Kang et al., 2019). $K_V2.1$-G379R channels exhibited loss of voltage-sensitivity and ion-selectivity, resulting in a non-specific cation leak current (Torkamani et al., 2014). When co-expressed with wild-type (WT) $K_V2.1$ subunits, $K_V2.1$-G379R exerted dominant-negative effects on potassium currents (Torkamani et al., 2014). However, the effect of $K_V2.1$-G379R on expression and subcellular distribution of $K_V2.1$ channels was not examined.

In the present study, we evaluated the effect of the DEE-associated *KCNB1*-p.G379R variant on $K_V2.1$ expression and clustering in HEK293T cells and observed a dominant negative effect on ER-PM clustering. To model this variant in vivo, we used CRISPR/Cas9 genome editing to generate a mouse model carrying the *KCNB1*-p.G379R pathogenic variant and characterized $K_V2.1$ expression and localization, as well as neurological, neurobehavioral, and cardiac phenotypes. *Kcnb1*^{G379R} mice exhibited spontaneous and handling-induced seizures, abnormal EEG patterns, profound hyperactivity, inattention/impulsivity, and

reduced anxiety-like behavior. The whole animal phenotype was more severe than that of a previously described global knockout allele (Speca et al., 2014). These mice recapitulate core features of *KCNB1*-associated DEE and will be a useful tool for understanding disease pathophysiology and evaluating potential therapies.

2. Materials and methods

2.1. HEK293T cell culture, immunocytochemistry, and epifluorescence and TIRF imaging

HEK293T cells were transfected with WT rat K_v2.1 in pRBG4, rat K_v2.1 S586A in pCGN, HA-tagged WT human K_v2.1, or HA-tagged WT human K_v2.1 with the G379R mutation (Shi et al., 1994; Lim et al., 2000; Kang et al., 2019). Cells were transiently transfected using Lipofectamine 2000 following the manufacturer's protocol within 18 h of plating. For immunocytochemistry, fixation was performed as previously described (Dickson et al., 2016; Kirmiz et al., 2018). Briefly, HEK293T cells were fixed in 3.2% formaldehyde, blocked and permeabilized. Cells were incubated in anti-HA epitope tag IgG2a mouse monocloncal antibody (mAb) 12CA5 (RRID:AB_ 2,532,070, pure, 5 μg/mL) and monoclonal anti-VAPA antibody N479/24 (RRID:AB_2,722,709, tissue culture supernatant 1:5). Coverslips were immunolabeled with Alexa-conjugated fluorescent IgG subclass-specific secondary antibodies (ThermoFisher; 1:1500) and Hoechst 33258 dye (ThermoFisher H1399; 200 ng/mL).

Epifluorescence and TIRF imaging of fixed cells and image analysis was performed essentially as described (Bishop et al., 2018; Kirmiz et al., 2018; Vierra et al., 2019). Images were obtained with an Andor iXon EMCCD camera installed on a TIRF/widefield equipped Nikon Eclipse Ti microscope using a Nikon LUA4 laser launch with 405, 488, 561 and 647 nm lasers and a 100× PlanApo TIRF/1.49 NA objective run with NIS Elements software (Nikon). Images were collected within NIS Elements as ND2 images.

2.2. Mice

Kcnb1$^{G379R/+}$ (abbreviated *Kcnb1*$^{R/+}$) mice on the C57BL/6J inbred strain were generated using CRISPR/Cas9 to introduce the modification of glycine 379 (same codon number in human and mouse) by homology directed repair. Three nucleotide changes were introduced, including two nucleotide changes in codon 379 (GGT > CGC) to maintain similar codon usage, and a silent change to disrupt an adjacent PAM site (C > A) (Fig. 1B). A single guide RNA (TAGATGTCTCCGTAACCAA NGG) with good targeting efficiency in Neuro2A cells and low predicted off-target effects, and a 200 bp repair oligo (5′-TCTCCAGCCTGGTCTTCTTTGCCGAGAAGGATGAGGATGACACCAAGTTCAAAAG CATCCCCGCCTCTTTCTGGTGGGCTACCATCACCATGACGACAGTTCGCTACGGAG ACATCTACCCTAAGACTCTCCTGGGGAAAATCGTGGGGGGCCTCTGTTGCATTGC CGGTGTCCTGGTGATTGCCCTCCCCATTCCAATT) were micro-injected into C57BL/6J embryos by the Northwestern University Transgenic and Targeted Mutagenesis Laboratory.

Potential founders were screened by PCR of genomic DNA using primers outside the repair oligo homology region (Table 1), and the region of interest was TOPO-cloned and Sanger sequenced (n = 12–22 clones per founder). The mosaic G379R founder was backcrossed to

C57BL/6J mice (Jackson Labs, #000664, Bar Harbor, ME) to generate N1 offspring. An additional founder heterozygous for a 2 bp deletion resulting in a frameshift (G379VfsTer6; abbreviated as *Kcnb1*$^{fs/+}$) was also bred similarly (Fig. 1B). N1 offspring were genotyped by Sanger sequencing to confirm transmission of the G379R editing event or the 2 bp deletion, and were screened for off-target events by Sanger sequencing of all potential sites with <3 mismatches. N1 mice with the confirmed on-target event and without off-target events were bred with C57BL/6J females to establish the lines, *Kcnb1*^{G379R} (*official allele designation:* *Kcnb1*^{em1Kea}) and *Kcnb1*^{fs} (2 bp deletion frameshift; official designation: *Kcnb1*^{em2Kea}), which are maintained by continual back-crossing of heterozygous mice with inbred C57BL/6J mice. Male and female *Kcnb1*$^{R/+}$ mice were intercrossed to generate *Kcnb1*$^{+/+}$ (WT), heterozygous *Kcnb1*$^{R/+}$, and homozygous *Kcnb1*$^{R/R}$ mice for experiments. Male and female *Kcnb1*$^{fs/+}$ mice were intercrossed to generated WT, *Kcnb1*$^{fs/+}$, and *Kcnb1*$^{fs/fs}$ mice; or crossed to C57BL/6J mice to generate WT and heterozygous *Kcnb1*$^{fs/+}$ mice for neurobehavioral experiments. For immunohistochemistry experiments, *Kcnb1*$^{-/-}$ knockout mice (*Kcnb1*^{tmDgen}) that we previously characterized were included for comparison (Speca et al., 2014).

Mice were maintained in a Specific Pathogen Free (SPF) barrier facility with a 14-h light/10-h dark cycle and access to food and water ad libitum. Both female and male mice were used for all experiments. All animal care and experimental procedures were approved by the Northwestern University and UC Davis Animal Care and Use Committees in accordance with the National Institutes of Health Guide for the Care and Use of Laboratory Animals. The principles outlined in the ARRIVE (Animal Research: Reporting of in vivo Experiments) guideline and Basel declaration (including the 3R concept) were considered when planning experiments.

2.3. Genotyping

DNA was isolated from tail biopsies using the Gentra Puregene Mouse Tail Kit according to the manufacturer's instructions (Qiagen, Valencia, CA). Genomic DNA was digested with BAMH1-HF (R3136, New England Biolabs, Ipswich, MA) at 37 °C for 1 h. Digested DNA was then diluted 1:1 with nuclease-free water and used for template for digital droplet PCR (ddPCR) using ddPCR Supermix for Probes (No dUTP) (Bio-Rad, Hercules, CA, USA) and custom TaqMan SNP Genotyping Assays (Life Technologies, Carlsbad, CA) to detect the mutations (Table 1). Reactions were partitioned into droplets in a QX200 droplet generator (Bio-Rad). PCR conditions were 95 °C for 10 min, then 44 cycles of 95 °C for 30 s and 60 °C for 1 min (ramp rate of 2 °C/s) and a final inactivation step of 98 °C for 5 min. Following amplification, droplets were analyzed with a QX200 droplet reader with QuantaSoft vl.6.6 software (Bio-Rad) (e.g., Fig. 1C).

2.4. Transcript analysis

Kcnb1 expression increases over the first 3 weeks of life and then stabilizes (Cardoso-Moreira et al., 2019). Whole brain RNA was extracted from 4 to 15-week-old WT, *Kcnb1*$^{R/+}$, *Kcnb1*$^{R/R}$, *Kcnb1*$^{fs/+}$ and *Kcnb1*$^{fs/fs}$ mice. Total RNA was isolated using TRIzol reagent according to the manufacturer's instructions (Invitrogen, Carlsbad, CA, USA). First-strand cDNA was synthesized from 2 to 4 micrograms of RNA using oligo(dT) primer and

Superscript IV reverse transcriptase (RT) according to the manufacturer's instructions (Life Technologies). First-strand cDNA samples were diluted 1:5 and 5 μL was used as template. Quantitative ddPCR was performed using ddPCR Supermix for Probes (No dUTP) (Bio-Rad) and TaqMan Gene Expression Assays (Life Technologies) for mouse *Kcnb1* (FAM-MGB-Mm00492791_m1) and *Tbp* (VIC-MGB-Mm00446971_m1) as a normalization standard. Reactions were partitioned into a QX200 droplet generator (Bio-Rad). Thermocycling conditions and analysis were performed as described for genotyping. Both assays lacked detectable signal in genomic, no-RT and no template controls. Relative transcript levels were expressed as a ratio of *Kcnb1* concentration to *Tbp* concentration, with 6–10 biological replicates per genotype. Statistical comparison between groups was made using ANOVA with Tukey's post-hoc comparisons (GraphPad Prism, San Diego, CA).

2.5. Immunoblotting

Whole brain membrane proteins were isolated from 4 to 15-week-old WT, $Kcnb1^{R/+}$, $Kcnb1^{R/R}$, $Kcnb1^{fs/+}$ and $Kcnb1^{fs/fs}$ mice. Membrane fractions ($Kcnb1^{G379R}$ samples for K_v2.1 blots: 50 μg/lane; $Kcnb1^{fs}$ samples for K_v2.1 blots: 100 μg/lane; All samples for K_v2.2 and AMIGO-1 blots: 100 μg/lane) were separated on a 7.5% SDS-PAGE gel and transferred to nitrocellulose. Blots were probed with anti-K_v2.1 mAbs ($Kcnb1^{G379R}$ samples - NeuroMab K89/34, RRID:10673392, pure, 2 μg/mL; $Kcnb1^{fs}$ samples - NeuroMab K39/25, RRID:2131649, pure, 10 μg/mL), anti-K_v2.2 mAb (NeuroMab N372B/1.1, RRID:2315869, tissue culture supernatant, diluted 1:2) or anti-AMIGO-1 mAb (NeuroMab L86/36.6, RRID: AB_2315799, tissue culture supernatant, diluted 1:2) and anti-mortalin/GRP75 mAb (NeuroMab N52A/42, RRID:2120479, pure, 1 μg/mL) which served as a normalization control. Alexa Fluor 790 and 680 goat anti-mouse antibodies (Jackson ImmunoResearch, 1:20,000) were used to detect signal on an Odyssey imaging system (Li-COR). Relative protein levels were determined by densitometry as previously described with ImageJ (NIH) (Rasband 1997-2018) or Image Studio (Li-COR) and expressed as a ratio of K_v2.1, K_v2.2 or AMIGO-1 to GRP75, with 5-7 biological replicates per genotype. Line scan analysis of K_v2.1 immunoblots was performed in ImageJ and expressed as the average ± SEM. Statistical comparison between groups was made using one-way ANOVA with Tukey's post-hoc comparisons (GraphPad Prism).

2.6. Immunohistochemistry

P24-25 WT, $Kcnb1^{R/+}$ and $Kcnb1^{R/R}$ mice were used for immunohistochemistry, while $Kcnb1^{fs}$ mice were not included in this analysis because epitopes for the immunolabeling-suitable K_v2.1 antibodies are all downstream of G379VfsTer6 frameshift. Animals were deeply anesthetized with pentobarbital and transcardially perfused with 4% formaldehyde prepared from paraformaldehyde, in 0.1 M sodium phosphate buffer pH 7.4 (0.1 M PB). Sagittal brain sections (30μm thick) were prepared and immunolabeled using free-floating methods as previously described (Rhodes et al., 2004; Speca et al., 2014; Palacio et al., 2017). Briefly, free floating sections were blocked and permeabilized. Sections were incubated with primary antibodies (see Table 2 for antibody details) and then immunolabeled with Alexa-conjugated fluorescent IgG subclass-specific secondary antibodies and Hoechst 33258 DNA stain at 200 ng/mL (ThermoFisher Cat# H21491). Images were taken using the same exposure time to compare the signal intensity directly.

Images were identically processed in Photoshop to maintain consistency between samples. For further details, see supplemental materials and methods.

2.7. Hippocampal neuron culture and immunocytochemistry

Immunostaining was performed on cultured hippocampal neurons isolated from WT, *Kcnb1*$^{R/+}$ and *Kcnb1*$^{R/R}$ mice. Detailed methods and images are presented in the supplement.

2.8. Seizure threshold testing

Male and female mice were tested between 9 and 12 weeks of age by experimenters blinded to genotype. Separate cohorts of mice were used for each inducing agent.

2.8.1. Flurothyl seizure induction

Susceptibility to seizures induced by the chemoconvulsant flurothyl (Bis(2,2,2-trifluoroethyl) ether, Sigma-Aldrich, St. Louis, MO) was assessed in WT, *Kcnb1*$^{R/+}$, *Kcnb1*$^{R/R}$, *Kcnb1*$^{fs/+}$ and *Kcnb1*$^{fs/fs}$ mice at P71-84. Flurothyl was introduced into a clear, plexiglass chamber (2.2 L) by a syringe pump at a rate of 20 μL/min and allowed to volatilize. Latencies to first myoclonic jerk, generalized tonic-clonic seizure (GTCS) with loss of posture, and time interval between these phases were recorded (n = 27-32 per genotype). Groups were compared using one-way ANOVA with Tukey's post-hoc comparisons for parametric data unless otherwise indicated (Table 3) (GraphPad Prism).

2.8.2. 6 Hz seizure induction

Susceptibility to 6 Hz psychomotor seizures was assessed in WT and *Kcnb1*$^{R/+}$ littermates at P67-89. Individual mice were subjected to 6 Hz of auricular stimulation (0.2 ms pulse width, 3 s duration) using an electroconvulsive unit (Ugo Basile, Gemonio (VA) Italy). Mice that did not exhibit a seizure on the first stimulation were subjected to a second stimulation (≥ 2 mA higher) separated by a delay of ≥15 min. Mice were scored for presence or absence of psychomotor seizure activity, defined as forelimb clonus, rearing, paddling or loss of posture. CC_{50} curves were calculated with n = 2–20 subjects per current stimulus. Stimulus response curves, CC_{50}, and respective confidence intervals (CI) were determined for each sex and genotype using log-probit analysis.

2.9. Video-EEG monitoring

Between P23-25, male and female WT, *Kcnb1*$^{R/+}$ and *Kcnb1*$^{R/R}$ mice were implanted with prefabricated 3-channel EEG headmounts (Pinnacle Technology, Lawrence, KS, USA). Briefly, mice were anesthetized with isoflurane or ketamine/xylazine and placed in a stereotaxic frame. Headmounts with four stainless steel screws that served as cortical surface electrodes were affixed to the skull with glass ionomer cement. Anterior screw electrodes were 0.5–1 mm anterior to bregma and 1mm lateral from the midline. Posterior screws were 4.5–5 mm posterior to bregma and 1 mm lateral from the midline. EEG1 represents recordings from right posterior to left posterior (interelectrode distance ≈2 mm). EEG2 represents recordings from right anterior to left posterior (interelectrode distance ≈5 mm). The left anterior screw served as the ground connection. Following at least 48 h of recovery,

tethered EEG and video data were continuously collected from freely moving mice with Sirenia acquisition software (Pinnacle Technology) as previously described (Hawkins et al., 2016). At least 216 h of EEG data were acquired from each subject (Range: WT: 216–504 h/mouse (n = 5 mice); *Kcnb1*$^{R/+}$: 216–504 h/mouse (n = 4 mice); *Kcnb1*$^{R/R}$: 360–32 h/mouse (n = 3 mice)). Raw data was notch filtered with a 1 Hz window around 60 and 120 Hz prior to analysis. Video-EEG records were analyzed with Persyst13 software (Persyst, Solana Beach, CA, USA), MATLAB (Math-Works, Massachusetts) and EEGLAB (Swartz Center for Computational Neuroscience, California) by a reviewer blinded to genotype. Epileptiform discharges were defined as isolated events with a spike and slow wave morphology, an amplitude of ≥3 times baseline, duration of 150–500 ms, and with increased power in frequencies >20 Hz compared to baseline. Samples with high baseline artifact were excluded from analysis.

2.10. Neurobehavioral assays

Male and female WT, *Kcnb1*$^{R/+}$, *Kcnb1*$^{R/R}$ and *Kcnb1*$^{fs/+}$ mice were tested between 11 and 15 weeks of age. Male and female mice were tested separately with at least a one-hour delay between sessions. For all experiments, mice were acclimated in the behavior suite with white noise for 1 h prior to behavioral testing. At the end of each procedure, mice were placed into a clean cage with their original littermates. Behavioral testing was performed by experimenters blinded to genotype. Evaluation occurred over 4 consecutive days: Day 1- neurological exam; Day 2- open field (OF); Day 3- zero maze; and Day 4-cliff avoidance. The marble burying assay was performed on a separate cohort of mice. Statistical comparison between groups were made using one-way ANOVA with Tukey's post-hoc comparisons for parametric data or two-way repeated measures ANOVA with Sidak's post-hoc comparisons, unless otherwise indicated (Table 3).

2.10.1. Neurological exam

Neurological assessment was based on a modified Irwin screen to evaluate baseline behavior (Irwin, 1968). Individual mice were placed in a small static cage for 3 min and observed for transfer behavior, body position, spontaneous activity, tremor, gait, pelvic elevation, tail elevation, palpebral closure, piloerection, air puff startle response, trunk curl, limb grasping, Preyer reflex, provoked salivation, and provoked biting. Each parameter was scored as shown in Table S1 and then summed for a total exam for each mouse. Total exam scores are shown with 23–32 mice per genotype.

2.10.2. Open field

Mice were evaluated for baseline activity in an open field. Individual mice were placed in the center of an open field arena (46 cm × 46 cm) and monitored for 10 min. Limelight software (Actimetrics, Wilmette, IL, USA) was used to video record each trial, track the position of the mouse, and calculate distance traveled and relative position in the arena (n = 21–30 mice per genotype).

2.10.3. Zero maze

Mice were evaluated for anxiety-related behavior in an elevated zero maze, a variant on the elevated plus maze that eliminates the ambiguous center region (Shepherd et al., 1994). Individual mice were placed near the closed arm of the maze and allowed to freely explore for 5 min. Limelight software was used to video record each trial, track the position of the mouse, and calculate time spent in closed or open arms and total distance traveled (n = 19–28 mice per genotype). Trials where mice jumped off the maze were excluded from the analysis.

2.10.4. Cliff Avoidance

Mice were evaluated for impulsive behavior using a cliff avoidance test. Individual mice were placed on an elevated platform (16 cm diameter, 25 cm height) for 7 min. Number of peering events (defined as the entire head extending over the edge of the platform) and fall/jumping events (defined as the entire body leaving the platform) were recorded. Jumping events were compared using time-to-event analysis, p-values were determined by LogRank Mantel-Cox tests (n = 15–29 per genotype).

2.10.5. Marble burying

Marble movement and burying were evaluated in WT, *Kcnb1*$^{R/+}$ and *Kcnb1*$^{R/R}$ mice to assess phenotypes related to anxiety- and obsessive-compulsive behavior. Individual mice were placed into a static rat cage with 5 cm of corncob bedding and acclimated for 15 min. Mice were then briefly removed from the cage while bedding was flattened and 20 marbles were evenly placed across the cage in 5 rows with 4 marbles each, with a small open space at the front of the cage. A baseline image of the cage was taken prior to reintroduction of the mouse and reimaged after the 30-min trial. The two images were compared for the number of marbles buried, defined by at least ½ of the marble being submerged under the bedding. Total number of marbles moved or buried were compared between groups by two-way repeated measures ANOVA with Sidak's multiple comparisons test (n = 9–25 mice per genotype).

2.11. Cardiac function

Preliminary screening of cardiac function in WT, *Kcnb1*$^{R/+}$ and *Kcnb1*$^{R/R}$ mice was performed with electrocardiography and echocardiography. Detailed methods and initial results are presented in the supplement (Supplemental Materials and Methods; Supplemental Figs. S1 and S2).

2.12. Statistical analysis

Table 3 summarizes statistical tests used for all comparison along with computed values. Values for post-hoc comparisons are reported in the results text and figure legends, and group n's are reported in figure legends. There were no significant differences between sexes on any measurements except 6 Hz seizure threshold. Thus, groups were collapsed across sex for all variables, except the 6 Hz seizure threshold.

3. Results

3.1. Kcnb1-p.G379R affects subcellular localization of K_V2.1 in HEK293T cells

Previous reports demonstrated that *KCNB1* pathogenic variants have altered expression and localization of K_V2.1 in CHO-K1 and COS-1 cell lines (Torkamani et al., 2014; Thiffault et al., 2015). Additionally, it was shown that rat K_V2.1 (rK_V2.1) exogenously expressed in HEK293T cells is specifically localized in large PM clusters similar to those seen in neurons (Trimmer, 1991; Scannevin et al., 1996; Mohapatra and Trimmer, 2006; Bishop et al., 2015; Fox et al., 2015; Johnson et al., 2018; Kirmiz et al., 2018). These clusters are located at and participate in ER-PM junctions that result from the interaction of K_V2.1 with ER proteins VAPA and VAPB (Fox et al., 2015; Johnson et al., 2018; Kirmiz et al., 2018). The clustering of K_V2.1 and recruitment of VAP proteins at ER-PM junctions is a non-conducting function of K_V2.1, which instead is dependent upon serine phosphorylation within the PRC domain, a small motif in the Kv2.1C-terminus (Lim et al., 2000; Johnson et al., 2018; Kirmiz et al., 2018). To determine whether the *Kcnb1-p.C379R* variant affected this non-conducting function of K_V2.1, we investigated human K_V2.1 (hK_V2.1) and hK_V2.1-G379R expression in HEK293T cells, which lack endogenous K_V2 channel expression even though they have attributes of a neuronal lineage (Yu and Kerchner, 1998; Shaw et al., 2002).

We first determined whether hK_V2.1 formed PM clusters and recruited VAPA proteins to ER-PM junctions in HEK293T cells. We used two imaging modalities to assess subcellular localization: conventional epifluorescence microscopy to evaluate overall expression pattern, and Total Internal Reflection Fluorescence (TIRF) microscopy to interrogate fluorescent signals within 100–200 nm of the cover slip. The “TIRF field” corresponded to the first ≈1% of the distance into the cell and primarily comprised the PM and PM-associated structures. Expression of hK_V2.1 in HEK293T cells localized to PM clusters in both epifluorescence and TIRF images, with the majority of hK_V2.1 present in the clusters (Fig 2A). Expression of hK_V2.1 led to a significant reorganization in the subcellular localization of VAPA relative to that seen in untransfected cells, such that VAPA was now enriched at K_V2.1-containing ER-PM junctions (Fig 2A). This colocalization of hK_V2.1 and VAPA was indicated by a relatively high Pearson’s Correlation Coefficient (PCC) of 0.7 (Fig. 2E). Expression of hK_V2.1-G379R in HEK293T cells suggested a primarily intracellular localization, with lack of concordance between epifluorescence images showing the entire cell and TIRF images showing the region at/near the PM (Fig. 2C). The hK_V2.1-G379R PCC value for colocalization with VAPA of 0.3 was lower than for hK_V2.1 ($p < 0.0001$) (Fig. 2E). Additionally cells expressing hK_V2.1-G379R had smaller average VAPA cluster size of 0.23 ± 0.02 μm^2 compared to cells expressing WT hK_V2.1 (0.63 ± 0.13 μm^2; $p = 0.0028$) (Fig. 2C,G).

The rK_V2.1-S586A mutation was previously shown to not recruit VAPA to ER-PM junctions (Kirmiz et al., 2018). As a control, we compared K_V2.1:VAPA co-localization and VAPA cluster size of rK_V2.1-S586A with WT hK_V2.1 or hK_V2.1-G379R. Consistent with our previous report, expression of rK_V2.1-S586A resulted in a lower PCC value of 0.28 ($p < 0.0001$) and smaller average VAPA cluster size of 0.18 ± 0.02 pm^2 ($p < 0.003$) compared to WT hK_V2.1 cluster size of 0.63 ± 0.13 μm^2 (Fig. 2B, E, G). Co-localization PCC values and

VAPA cluster sizes were not different between $hK_v2.1$ and $rK_v2.1$, or $hK_v2.1$-G379R and $rK_v2.1$-S586A mutants (Fig. 2E, G). As an additional control, $rK_v2.1$ and $hK_v2.1$-G379R were co-expressed and found to have similar localization and size properties of the $hK_v2.1$-G379R mutation alone, suggesting G379R may exert a dominant negative effect on co-expressed $K_v2.1$ (Fig. 2E–G). This is consistent with the previously reported dominant negative effect of G379R on $K_v2.1$ conducting functions (Torkamani et al., 2014). Based on the complexity of the G379R dominant-negative cellular phenotypes, it is difficult to predict effects on neurophysiology; therefore, we generated a mouse model.

3.2. Generation and initial characterization of Kcnb1^{G379R} mice

To model the DEE-associated *KCNB1*-p.G379R pathogenic variant in vivo, we used CRISPR/Cas9 genome editing to introduce the G379R missense variant in the mouse *Kcnb1* gene by homology directed repair. *Kcnb1*$^{G379R/+}$ heterozygous and *Kcnb1*$^{G379R/G379R}$ homozygous mutants (abbreviated as *Kcnb1*$^{R/+}$ and *Kcnb1*$^{R/R}$, respectively) were born at the expected Mendelian ratios. As a by-product of genome editing, we also obtained a 2 bp deletion allele resulting in a frameshift. Heterozygous and homozygous mice carrying the G379VfsTer6 frameshift allele (abbreviated *Kcnb1*$^{fs/+}$ and *Kcnb1*$^{fs/fs}$, respectively) were also born at the expected Mendelian ratios. Droplet digital RT-PCR (RT-ddPCR) evaluating whole brain *Kcnb1* transcript indicated no expression difference between WT, *Kcnb1*$^{R/+}$ and *Kcnb1*$^{R/R}$ mice (Fig. 3A). There was a modest elevation in transcript for *Kcnb1*$^{fs/+}$ ($p = 0.004$) and *Kcnb1*$^{fs/fs}$ ($p = 0.0004$) mice relative to WT littermates (Fig. 3E).

3.3. Lower $K_v2.1$ channel expression in Kcnb1^{G379R} mice

To evaluate the effect on $K_v2.1$ protein expression, we first performed immunoblotting using whole brain membrane preparations from *Kcnb1*^{G379R} and *Kcnb1*^{fs} lines. These analyses revealed that whole brain expression of $K_v2.1$ was ≈15% lower in *Kcnb1*$^{R/+}$ ($p < 0.005$) heterozygotes and ≈67% lower in *Kcnb1*$^{R/R}$ ($p < 0.0001$) homozygous mice compared to WT littermates (Fig. 3B–C). There was also an evident shift in the relative electrophoretic mobility (M_r) from the fully post-translationally modified form (≈125 kDa) of $K_v2.1$ toward an M_r of ≈96 kDa, suggesting a deficit in the processing of the *Kcnb1*^{G379R} variant into the mature, fully post-translationally modified species (Fig. 3B, D) (Murakoshi et al., 1997; Misonou et al., 2004). Immunoblotting analysis of the *Kcnb1*^{fs} line with an antibody targeting an epitope upstream of the frameshift (Table 2) revealed that $K_v2.1$ expression was ≈45% lower in *Kcnb1*$^{fs/+}$ ($p = 0.0001$) and ≈89% lower in *Kcnb1*$^{fs/fs}$ ($p < 0.0001$) mice compared to WT littermates (Fig. 3F,G). This was similar to the level of expression observed with a *Kcnb1*$^{-/-}$ knockout control, which had ≈85% lower expression compared to WT. This suggests that the residual signal is non-specific and that the *Kcnb1*^{fs} line is comparable to a knockout line.

To assess the impact of the *Kcnb1*^{G379R} variant on neuroanatomy and $K_v2.1$ expression, we performed immunolabeling of brain sections from WT, *Kcnb1*$^{R/+}$ and *Kcnb1*$^{R/R}$ mice. The *Kcnb1*^{G379R} variant had no overt effect on gross hippocampal neuroanatomy based on labeling with the DNA-specific dye Hoechst 33258 (data not shown), which was similar to previous observations in *Kcnb1*$^{-/-}$ mice (Speca et al., 2014). $K_v2.1$ immunolabeling (green) in hippocampal, subicular and neocortical neurons in *Kcnb1*$^{R/+}$ mice was lower in intensity

compared to WT (Fig. 4A–C). *Kcnb1*$^{R/R}$ mice had little detectable K_v2.1 immunolabeling (Fig. 4A–C), and substantially reduced immunolabeling for K_v2.2 and AMIGO-1. This was qualitatively consistent with immunoblotting results (Fig. 3B, C) and results obtained with cultured hippocampal neurons (Supplemental Fig. S3). To ensure specificity of the K_v2.1 antibody, we also immunolabeled *Kcnb1*brain sections, which lacked detectable K_v2.1 signal (Fig. 4C). As previously reported (Speca et al., 2014), the pattern and intensity of K_v2.2 immunolabeling in the *Kcnb1*$^{-/-}$ brain sections was comparable to that in WT sections (Fig. 4C). Notably, when we enhanced the intensity of *Kcnb1*$^{R/R}$ images, the remaining signal was found to be predominantly K_v2.2 and AMIGO-1 (Fig. 4C) such that the enhanced images resembled the non-enhanced image from the *Kcnb1*$^{-/-}$ brain sections (Fig. 4C'). Additional validation of lower K_v2.1 expression due to the *Kcnb1*^{G379R} variant was performed by immunolabeling with three additional K_v2.1 antibodies each recognizing a distinct region of K_v2.1, D3/71R, L105/31 and L80/21 (Table 2), each of which detected a similarly low level of K_v2.1 immunolabeling (Supplemental Fig. S4).

Kcnb1^{G379R} also affected expression of K_v2.2 and the K_v2 channel auxiliary subunit AMIGO-1. Immunolabeling experiments performed on WT, *Kcnb1*$^{R/+}$ and *Kcnb1*$^{R/R}$ brain sections revealed lower K_v2.2 and AMIGO-1 expression in *Kcnb1*$^{R/R}$ versus WT mice (Fig. 4A–C). To quantitate the effect of the *Kcnb1*^{G379R} variant on K_v2.2 and AMIGO-1 protein expression, immunoblotting was performed on whole brain membrane preparations (Fig. 4D–G). Immunoblotting showed that whole brain expression of K_v2.2 was ≈30% lower in *Kcnb1*$^{R/+}$ ($p < 0.05$) and ≈50% lower in *Kcnb1*$^{R/R}$ mice ($p < 0.002$) compared to WT littermates (Fig. 4D, E). Immunoblotting for AMIGO-1 whole brain expression revealed ≈25% lower expression in *Kcnb1*$^{R/+}$ and ≈47% lower expression in *Kcnb1*$^{R/R}$ mice ($p < 0.004$) compared to WT littermates (Fig. 4F, G). This is consistent with a dominant negative effect on K_v2 channel complexes.

3.4. Lower threshold for induced seizures in Kcnb1^{G379R} mice

In order to examine seizure sensitivity, we evaluated response of *Kcnb1*^{G379R} mice to the volatile chemoconvulsant flurothyl, a $GABA_A$ antagonist (van Vliet et al., 2017). Latency to the first myoclonic jerk did not differ between genotypes, while latency to the first generalized tonic-clonic seizure (GTCS) with loss of posture was affected by genotype (Table 3). GTCS latency was lower in *Kcnb1*$^{R/R}$ compared to either WT ($p < 0.0001$) or *Kcnb1*$^{R/+}$ mice ($p = 0.0004$). *Kcnb1*$^{R/+}$ mice also had a lower GTCS threshold than WT mice ($p = 0.0477$). Average latency was 112 ± 5 s for *Kcnb1*$^{R/R}$ mice, 153 ± 8 s for *Kcnb1*$^{R/+}$ mice, and 178 ± 8 s for WT littermates (Fig. 5A). Time to progress from the first myoclonic jerk to GTCS was affected by genotype (Table 3), with both *Kcnb1*$^{R/R}$ and *Kcnb1*$^{R/+}$ mice progressing more rapidly between stages compared to WT ($p = 0.0040$ and $p = 0.0438$, respectively) (Fig. 5B). Average progression time was 28 ± 7 s for *Kcnb1*$^{R/R}$, 49 ± 9 s for *Kcnb1*$^{R/+}$ and 68 ± 8 s for WT. In order to compare flurothyl susceptibility of *Kcnb1*$^{R/+}$ and *Kcnb1*$^{R/R}$ mice to the heterozygous and homozygous null condition, we ran a concurrent cohort of *Kcnb1*^{fs} mice. Under our experimental conditions, the *Kcnb1*^{fs} alleles did not differ from WT littermates in flurothyl sensitivity measurements, including latencies to MJ, GTCS, or time progression between the two (Table 3) (Fig. 5A–B). Although this differs from the enhanced flurothyl susceptibility previously reported for *Kcnb1*$^{-/-}$ mice

(Speca et al., 2014), the protocol used here had faster introduction of flurothyl, which is less likely to detect small effects on threshold.

We next investigated whether *Kcnb1*^{G379R} influenced latency to psychomotor seizures induced by long duration, low frequency stimulation (6 Hz, 3 s), a model of pharmacoresistant focal seizures (van Vliet et al., 2017). *Kcnb1*$^{R/+}$ heterozygotes and WT littermates were subjected to 6 Hz stimulation and scored for the presence or absence of seizure activity (forelimb clonus, rearing, paddling or loss of posture). Convulsive current (CC) curves were generated as previously described (Finney, 1971), and population CC_{50} values (CC at which 50% of mice seized) were determined for each genotype and sex. Both male and female *Kcnb1*$^{R/+}$ mice had lower CC_{50} values compared to sex-matched WT controls ($p < 0.0001$) (Fig. 5C). The CC_{50} values (95% confidence interval) for WT and *Kcnb1*$^{R/+}$ male mice were 23.7 mA (19.5 to 27.9) and 16.4 mA (14.3 to 18.6), respectively. The CC_{50} values for WT and *Kcnb1*$^{R/+}$ female mice were 18.7 mA (16.5 to 20.9) and 16.2 mA (13.3 to 19.1), respectively.

3.5. Handling-induced seizures in Kcnb1^{G379R} mice

We initially observed during the course of routine husbandry that *Kcnb1*^{G379R} mice exhibited seizures following handling, as well as overt home cage hyperactivity, repetitive jumping, and rare unexpected deaths in otherwise healthy appearing animals (median age at death P27, range P21-172). Based on these initial observations of seizures, we systematically assessed handling-induced behavioral seizures once per week between 6 and 12 weeks of age by individually transferring mice to clean cages and observing for 1 min. During those observations, 42% (10 of 24) *Kcnb1*$^{R/R}$ mice exhibited behavioral seizures with forelimb clonus, rearing and falling, sometimes followed by wild running (Fig. 5D) (Supplemental Video S1). In contrast, *Kcnb1*$^{R/+}$ heterozygous mice (n = 23) and WT littermates (n = 23) did not exhibit any seizures during these observations ($p < 0.001$) (Fig. 5D). Similar handling-induced seizures were observed infrequently in *Kcnb1*$^{R/+}$ heterozygotes, but at older ages (>4 months).

3.6. EEG abnormalities in Kcnb1^{G379R} mice

The behaviors observed during handling-induced seizures described above were similar to behaviors coinciding with spontaneous generalized tonic-clonic seizures during video-EEG monitoring of *Kcnb1*$^{R/R}$ mice at 3 to 6 weeks of age (Fig. 6A; Supplemental Video S2–S2a). Unprovoked spontaneous seizures occurred rarely (one to two times per animal during monitoring period; average frequency of <1 per week) in *Kcnb1*$^{R/R}$ mice (Fig. 6A), but were never observed in WT or *Kcnb1*$^{R/+}$mice. In addition, homozygous *Kcnb1*$^{R/R}$ mice displayed recurrent, brief runs of rhythmic slow spike and wave complexes (1–2 Hz) that lasted up to a minute during wakefulness or up to 15 min during sleep (Fig. 6B–C; Supplemental Videos S3–S4). Several types of interictal EEG abnormalities were obseived (Fig. 7). Both *Kcnb1*$^{R/+}$ and *Kcnb1*$^{R/R}$ mice exhibited isolated spike and slow wave complexes (Fig. 7B–D; Supplemental Video S5) that have an increase in power across low and high frequencies up to 170 Hz (Fig. 7E). The occurrence of the isolated spike and slow wave complexes was elevated relative to WT littermates (Fig. 7F) when quantified over a 24-h period.

3.7. Neurological abnormalities in Kcnb1^{G379R} mice

A neurological exam was used to evaluate baseline neurological function in 3 week old WT, *Kcnb1*$^{R/+}$ and *Kcnb1*$^{R/R}$ mice, including analysis of muscle, spinocerebellar, sensory, neuropsychiatric and autonomic functions (Irwin, 1968). *Kcnb1*$^{fs/+}$ mice were included as control to contrast *Kcnb1*$^{R/+}$ to the heterozygous null condition, as heterozygosity is the genotype present in *KCNB1* DEE patients. Neurological exam scores were affected by *Kcnb1* genotype, with higher scores indicating deficits. *Kcnb1*$^{R/+}$ had an average overall exam score of 17.2 ± 0.4, that was elevated ($p = 0.0004$) compared to the WT control score of 15.1 ± 0.4 (Fig. 8A). *Kcnb1*$^{R/R}$ mice had the highest score, with an average of 19.8 ± 0.5 ($p < 0.0001$ vs WT, *Kcnb1*$^{R/+}$ and *Kcnb1*$^{fs/+}$, respectively) (Fig. 8A). In contrast, *Kcnb1*$^{fs/+}$ mice had an average score of 16.2 ± 0.3 that did not differ from WT littermates ($p = 0.1372$). Differences in the overall exam score in *Kcnb1*^{G379R} mice were driven largely by differences in activity levels, escape behavior, and trunk curl (Supplemental Table S1). Furthermore, it was noted that upon transfer into the observation cage, 2 of 23 *Kcnb1*$^{R/R}$ mice exhibited a tonic-clonic seizure characterized by bilateral forelimb clonus with rearing and falling.

3.8. Kcnb1^{G379R} mice exhibit profound hyperactivity

Kcnb1^{G379R}mice were easily distinguishable from WT littermates in home cages based on their elevated activity level. Baseline activity measured in an open field assay showed that *Kcnb1*$^{R/+}$ mice traveled farther than WT controls, with average distances of 59.3 ± 2.2 m and 45.6 ± 2.0 m, respectively ($p = 0.0003$). *Kcnb1*$^{fs/+}$ mice traveled 52.0 ± 2.2 m, which did not differ from WT (Fig. 8B). *Kcnb1*$^{R/R}$ mice spent the majority of the session moving around the perimeter of the arena, traveling an average distance of 75.8 ± 3.1 m, more than WT controls, *Kcnb1*$^{R/+}$ and *Kcnb1*$^{fs/+}$ mice ($p < 0.0001$, $p < 0.0001$, $p < 0.0001$, respectively; Fig. 8B, C, J). *Kcnb1*$^{R/R}$ mice spent <5% of their time in the center of the arena compared to WT, *Kcnb1*$^{R/+}$ and *Kcnb1*$^{fs/+}$ mice ($p = 0.0011$, $p = 0.0001$, $p = 0.0003$, respectively) that all spent —10% of the time in the center (Fig. 8C, H–J).

3.9. Impulsivity and diminished anxiety-related behaviors in Kcnb1^{G379R} mice

Along with their noticeably elevated activity, *Kcnb1*^{G379R} mice appeared to have altered impulsivity/anxiety-like behavior. To further assess these behavioral abnormalities, we used zero-maze, cliff avoidance and marble burying assays. The zero-maze assay evaluated anxiety-related behavior of WT and *Kcnb1* mutants by comparing time spent in open versus closed arms. *Kcnb1*$^{R/+}$ mice spent an average of 38.6 ± 1.3% of the test time in open arms compared to WT controls that averaged 31.4 ± 1.9% of time ($p = 0.0100$) (Fig. 8D). *Kcnb1*$^{R/R}$ mice spent more than half their time (55.7 ± 2.3%) in the open arms of the maze, more than WT, *Kcnb1*$^{R/+}$ or *Kcnb1*$^{fs/+}$ mice ($p < 0.0001$, respectively) (Fig. 8D). *Kcnb1*$^{fs/+}$ mice spent 35.4 ± 1.1% of their time in the center, which did not differ from WT ($p = 0.2749$). Distance traveled in the zero-maze differed between *Kcnb1* genotypes and mirrored the effects seen in open field distance traveled (Fig. 8B, E). In this assay, distance traveled for *Kcnb1*$^{fs/+}$ mice was similar to *Kcnb1*$^{R/+}$ mice and both were greater than WT ($p = 0.005$, $p < 0.03$, respectively) (Fig. 8E).

The cliff avoidance assay takes advantage of the natural tendency of mice to avoid a potential fall from a height and is used to assess inattentive and impulsive behavior (Matsuoka et al., 2005; Yamashita et al., 2013). WT, *Kcnb1*^{G379R} and *Kcnb1*$^{fs/+}$ mice were individually placed on an elevated platform and monitored for jumping or stepping off the platform. Most WT mice ≈85%; 22 of 26) remained on the platform for the duration of the test, and *Kcnb1*$^{fs/+}$ performed similarly ≈80%; 12 of 15) (Fig. 8F). Fewer *Kcnb1*$^{R/+}$ ≈48%; 14 of 29) and *Kcnb1*$^{R/R}$ (≈22%; 5 of 23) remained on the platform compared to WT littermates ($p = 0.0088$ and $p < 0.0001$, respectively). Furthermore, *Kcnb1*$^{R/R}$ mice left the platform more often than *Kcnb1*$^{R/+}$ or *Kcnb1*$^{fs/+}$ mice ($p = 0.0052$, $p = 0.0006$, respectively) (Fig. 8F).

The marble burying assay assessed attention, anxiety, and obsessive-compulsive related behaviors of WT and *Kcnb1*^{G379R} mutants. Relative to WT controls, *Kcnb1*$^{R/R}$ mice showed little interaction with the marbles, moving few and failing to bury any ($p = 0.0225$) (Fig. 8G).

4. Discussion

KCNB1-p.G379R was identified as a pathogenic de novo variant in a child with DEE. Electrophysiological studies of $K_v2.1$ channels with the G379R variant in a heterologous expression system demonstrated lower potassium conductance relative to WT, loss of ion selectivity, and gain of a depolarizing inward cation currents (Torkamani et al., 2014). In addition, mutant subunits exerted a dominant negative effect on potassium currents when co-expressed with WT subunits (Torkamani et al., 2014). We extended in vitro characterization of the *Kcnb1*-p.C379R variant by demonstrating failure of $K_v2.1$-G379R to induce ER-PM junctions, as well as dominant negative effects on co-expressed WT $K_v2.1$ subunits. Together, these results suggest that *KCNB1*-p.G379R exerts dominant negative effects on both conducting and non onducting $K_v2.1$ functions. Introduction of this variant in *Kcnb1*^{G379R} knock-in mice provides a new model of *KCNB1*-associated DEE. This model recapitulates several key features of the human disorder, including seizures, interictal epileptiform events on EEG, behavioral hyperactivity, impulsivity/inattention, and attenuated anxiety-related behavior. Additionally, we show that *Kcnb1*^{G379R} results in a more severe phenotype than a frameshift allele that had loss of $K_v2.1$ similar to the global knock-out allele (Speca et al., 2014).

The proband with the *KCNB1*-p.C379R de novo variant initially presented with infantile spasms at 8 months of age and later developed multiple seizure types including focal dyscognitive, atonic, and generalized tonic-clonic seizures (Torkamani et al., 2014). Seizures were difficult to treat and adequate control was not achieved with ACTH, topiramate, valproic acid, pyridoxine, or the ketogenic diet. EEG findings at different time points included hypsarrhythmia, diffuse polyspikes, diffuse polyspike and slow-waves, right temporal spike and waves, and left occipital spikes. Beyond seizures, there was also developmental delay and an autism spectrum disorder diagnosis consistent with atypical Rett syndrome (Torkamani et al., 2014; Srivastava et al., 2018). The *Kcnb1*^{G379R} mouse model shares a number of these key phenotypes and will be a useful platform for evaluation of potential therapies for *KCNB1*-associated DEE.

Electrographic and behavioral seizures in *Kcnb1*^{G379R} mice shared features of seizures seen in the proband (Torkamani et al., 2014). The *Kcnb1*^{G379R} mice exhibited generalized tonic-clonic seizures that occurred both spontaneously and with brief handling. Handling-induced seizures are akin to reflex seizures, which are included as equivalent to unprovoked seizures in the ILAE definition of epilepsy (Fisher et al., 2014). Numerous EEG abnormalities were noted in *Kcnb1*^{G379R} mice, including isolated spike and slow waves and recurrent runs of rhythmic slow spike and wave complexes lasting up to 15 min without a behavioral correlate. These events and features will be useful biomarkers to evaluate potential therapeutic strategies that can normalize the EEG.

Neurobehavioral abnormalities were prominent in the *Kcnb1*^{G379R} mice and share some overlap with features reported in children with *KCNB1*-associated DEE (Torkamani et al., 2014; Thiffault et al., 2015; Calhoun et al., 2017; de Kovel et al., 2017; Marini et al., 2017; Srivastava et al., 2018; Bar, 2020). Attention-deficit/hyperactivity disorder or hyperactivity with inattention has been reported in numerous cases of *KCNB1*-associated DEE. *Kcnb1*^{G379R} mice exhibit profound hyperactivity both in their home and novel environments, and inattention was suggested by failure to interact with marbles in the marble burying assay. In addition, lack of preference for the closed arms in the zero maze could be due to inattention to surroundings and/or reduced anxiety-like behavior. Failure of the cliff avoidance response in *Kcnb1*^{G379R} mice may reflect inattention and/or elevated impulsivity, another behavioral problem reported for individuals with *KCNB1*-associated DEE. Although visual deficits could explain the observed inattention, there was no deficit in visual placing in *Kcnb1*^{G379R} mice and prior characterization of *Kcnb1*$^{-/-}$ mice included assessment of vision, which detected no impairment (Speca et al., 2014). Autism spectrum disorder has been reported in more than half of *KCNB1*-associated DEE cases, including *KCNB1*-p.G379R. Repetitive jumping was another prominent behavior observed in the *Kcnb1* mice in their home cages and upon transfer to a novel environment. This perseverative behavior was also previously reported in the *Kcnb1*$^{-/-}$ mice and may reflect repetitive movements seen in *KCNB1* DEE patients with autism spectrum disorder (Speca et al., 2014).

Previous work demonstrated that global homozygous deletion of *Kcnb1* in mice resulted in pronounced hyperactivity, reduced anxiety-like behavior, and enhanced susceptibility to flurothyl and pilocarpine-induced seizures (Speca et al., 2014). The neurobehavioral phenotypes of *Kcnb1*$^{R/R}$ mice were qualitatively similar to those reported for *Kcnb1*$^{-/-}$ on the same C57BL/6 J background strain. However, parallel comparison of *Kcnb1*$^{R/+}$ and *Kcnb1*$^{fs/+}$ mice in a subset of neurobehavioral assays suggests that G379R is more severe than the G379VfsTer6 frameshift allele that did not differ from WT. Furthermore, seizure phenotypes are more prominent in *Kcnb1*^{G379R} mice relative to *Kcnb1*^{fs} and *Kcnb1*$^{-/-}$ global knock-out mice (Speca et al., 2014). Seizure activity was reported in ≈10% of homozygous *Kcnb1*$^{-/-}$ mice during the course of routine handling (Speca et al., 2014). This is similar to the frequency of handling-induced seizure activity observed in heterozygous *Kcnb1*$^{R/+}$ mice, while seizures were observed in almost half of homozygous *Kcnb1*$^{R/R}$ mice between 6 and 12 weeks of age. Direct comparison of flurothyl sensitivity showed that both *Kcnb1*$^{R/+}$ and *Kcnb1*$^{R/R}$ mice had lower GTCS thresholds and faster MJ-GTCS transitions relative to WT, while *Kcnb1*^{fs} mice did not differ from WT. This provides further evidence

of a more severe phenotype with the *Kcnb1*^{G379R} allele. In vitro functional studies of *Kcnb1*-p.C379R showed change of function effects including loss of voltage-sensitivity and altered ion-selectivity, as well as dominant negative effects when co-expressed with WT subunits (Torkamani et al., 2014). In addition to alterations in the biophysical properties of K_v2.1 channels, the G379R mutation also appeared to exert a dominant negative influence on the expression and subcellular localization of WT K_v2.1, and transdominant negative effects on expression of K_v2.2 and AMIGO-1 subunits. Immunohistochemistry and immunoblotting experiments revealed that immunoreactivity for both K_v2.2 and AMIGO-1 was lower in sections and whole brain membrane preparations from *Kcnb1*$^{R/R}$ mice compared to both WT mice and to *Kcnb1*null mice. K_v2.1 and K_v2.2 are colocalized in some neuron types (e.g., Satb2-positive cells in layer 5 cortex) and form heteromeric channels, with most complexes also containing AMIGO-1 auxiliary subunits (Kihira et al., 2010; Peltola et al., 2011; Bishop et al., 2018). It is possible that effects on heteromeric channels that include the *Kcnb1*^{G379R} mutant may contribute to the more severe seizure phenotypes observed in *Kcnb1*G379R mice as compared to *Kcnb1*$^{-/-}$ null mice, which had normal expression of K_v2.2 (Speca et al., 2014). Future studies will investigate the neurophysiological basis of seizure phenotypes in *Kcnb1*^{G379R} mice.

Beyond neurological phenotypes, there have been anecdotal reports of borderline long QT syndrome in patients with *KCNB1*-associated encephalopathy (Kcnb1.org). Additionally, *KCNB1* is highly expressed in mouse cardiac tissue and synonymous SNPs in *KCNB1* have been associated with long QT syndrome in humans (Iwasa et al., 2001). Our preliminary evaluation of cardiac phenotypes suggested that homozygous *Kcnb1*$^{R/R}$ mice had prolonged QT_c interval relative to WT at baseline and following an isoproterenol challenge (Supplemental Fig. S1). There was no evidence of structural abnormalities or contractile dysfunction by ECHO (Supplemental Fig. S2 & Table S2). *KCNB1* variants could conceivably contribute to spontaneous or induced cardiac arrhythmia (e.g., exposure to proarrythmic drugs), although future studies will be required to further characterize the arrhythmogenic potential of *Kcnb1*^{G379R}.

In summary, we developed a novel knock-in mouse model of human DEE caused by a missense mutation in *Kcnb1* that disrupts both conducting and non-conducting functions of K_v2.1 channels. The *Kcnb1*^{G379R} mouse model will be valuable for defining the molecular and neurophysiological consequences of *Kcnb1* mutation, understanding disease pathophysiology, and evaluating response to therapeutic interventions.

Supplementary Material

Refer to Web version on PubMed Central for supplementary material.

Acknowledgements

We thank Alexandra Huffman and Nicole J. Zachwieja for technical assistance. The genetically engineered mice were generated with the assistance of Lynn Doglio in Northwestern University Transgenic and Targeted Mutagenesis Laboratory. Echocardiography was performed by Veronica Ramirez in the Cardiovascular Phenotyping Core of the Feinberg Cardiovascular and Renal Research Institute. Cultured neuron imaging was performed at the Northwestern University Center for Advanced Microscopy generously supported by NCI CCSG P30 CA060553 awarded to the Robert H Lurie Comprehensive Cancer Center. Sunita Misra was supported by a Lurie Children's

Hospital Pediatric Physician Scientist Research Award and National Institutes of Health grant 2KL2 TR001424-05A1. Lisa Wren was supported by an American Heart Association Predoctoral Fellowship. This work was supported by the National Institutes of Health grants R01 NS053792 (JAK), R01 NS114210 (JST), F32 NS108519 (NCV) and U54 NS108874 (ALG).

Abbreviations:

ACTH	adrenocorticotropic hormone
ADHD	attention deficit hyperactivity disorder
ANOVA	analysis of variance
Cas9	CRISPR associated protein 9
CC	convulsive current
CI	confidence interval
CRISPR	Clustered Regularly Interspaced Short Palindromic Repeats
ddPCR	droplet digital polymerase chain reaction
DEE	developmental and epileptic encephalopathy
ECG	electrocardiogram
ECHO	echocardiogram
EEG	electroencephalogram
ER	endoplasmic reticulum
Flurothyl	Bis(2,2,2-trifluoroethyl) ether
mAb	monoclonal antibobdy
PAM	protospacer adjacent motif
PCC	Pearson’s Correlation Coefficient
PCR	polymerase chain reaction
PM	plasma membrane
RT-PCR	reverse transcription polymerase chain reaction
SPF	specific pathogen free
WT	wild-type

References

Allen NM, et al., 2016 Unexplained early onset epileptic encephalopathy: exome screening and phenotype expansion. Epilepsia 57, e12–e17. [PubMed: 26648591]

Bar C, et al., 2020 Expanding the genetic and phenotypic relevance of KCNB1 variants in developmental and epileptic encephalopathies: 27 new patients and overview of the literature. Hum. Mutat 41 (1), 69–80. 10.1002/humu.23915,31513310 [PubMed: 31513310]

Berg AT, et al., 2010 Revised terminology and concepts for organization of seizures and epilepsies: report of the ILAE commission on classification and terminology, 2005–2009. Epilepsia 51, 676–685. [PubMed: 20196795]

Bishop HI, et al., 2015 Distinct cell- and layer-specific expression patterns and independent regulation of Kv2 channel subtypes in cortical pyramidal neurons. J. Neurosci 35, 14922–14942. [PubMed: 26538660]

Bishop HI, et al., 2018 Kv2 ion channels determine the expression and localization of the associated AMIGO-1 cell adhesion molecule in adult brain neurons. Front. Mol. Neurosci 11.

Calhoun JD, et al., 2017 Characterization of a KCNB1 variant associated with autism, intellectual disability, and epilepsy. Neurol Genet. 3, e198. [PubMed: 29264390]

Cardoso-Moreira M, et al., 2019 Gene expression across mammalian organ development. Nature 571, 505–509. [PubMed: 31243369]

de Kovel CF, et al., 2017 Neurodevelopmental disorders caused by de novo variants in Kcnb1 genotypes and phenotypes. JAMA Neurol. 74, 1228–1236. [PubMed: 28806457]

Dickson EJ, 2017 Endoplasmic reticulum-plasma membrane contacts regulate cellular excitability. Adv. Exp. Med. Biol 997, 95–109. [PubMed: 28815524]

Dickson EJ, et al., 2016 Dynamic formation of ER-PM junctions presents a lipid phosphatase to regulate phosphoinositides. J. Cell Biol 213, 33–48. [PubMed: 27044890]

Du J, et al., 1998 The K+ channel, Kv2.1, is apposed to astrocytic processes and is associated with inhibitory postsynaptic membranes in hippocampal and cortical principal neurons and inhibitory interneurons. Neuroscience 84, 37–48. [PubMed: 9522360]

Finney, 1971 Probit Analysis. J. Pharm. Sci 60, 1432.

Fisher RS, et al., 2014 ILAE official report: a practical clinical definition of epilepsy. Epilepsia 55, 475–482. [PubMed: 24730690]

Fox PD, et al., 2015 Induction of stable ER-plasma-membrane junctions by Kv2.1 potassium channels. J. Cell Sci 128, 2096–2105. [PubMed: 25908859]

Fu J, et al., 2017 Kv2.1 clustering contributes to insulin exocytosis and rescues human β-cell dysfunction. Diabetes. 66, 1890–1900. [PubMed: 28607108]

Gallo A, et al., 2016 Endoplasmic reticulum-plasma membrane associations: structures and functions. Annu. Rev. Cell Dev. Biol 32, 279–301. [PubMed: 27298092]

Guan D, et al., 2007 Kv2 subunits underlie slowly inactivating potassium current in rat neocortical pyramidal neurons. J. Physiol 581, 941–960. [PubMed: 17379638]

Hawkins NA, et al., 2016 Fine mapping of a Dravet syndrome modifier locus on mouse chromosome 5 and candidate gene analysis by RNA-Seq. PLoS Genet 12, e1006398. [PubMed: 27768696]

Henne WM, et al., 2015 Molecular mechanisms of inter-organelle ER-PM contact sites. Curr. Opin. Cell Biol 35, 123–130. [PubMed: 26025028]

Hönigsperger C, et al., 2017 Physiological roles of Kv2 channels in entorhinal cortex layer II stellate cells revealed by Guangxitoxin-IE. J. Physiol 595, 739–757. [PubMed: 27562026]

Irwin S, 1968 Comprehensive observational assessment: Ia. A systematic, quantitative procedure for assessing the behavioral and physiologic state of the mouse. Psychopharmacologia 13, 222–257. [PubMed: 5679627]

Iwasa H, et al., 2001 Multiple single-nucleotide polymorphisms (SNPs) in the Japanese population in six candidate genes for long QT syndrome. J. Hum. Genet 46, 158–162. [PubMed: 11310586]

Johnson B, et al., 2018 Kv2 potassium channels form endoplasmic reticulum/plasma membrane junctions via interaction with VAPA and VAPB. Proc. Natl. Acad. Sci 115, E7331–E7340. [PubMed: 29941597]

Kang SK, et al., 2019 Spectrum of KV 2.1 dysfunction in KCNB1-associated neurodevelopmental disorders. Ann. Neurol 86, 899–912. [PubMed: 31600826]

Kihira Y, et al., 2010 Formation of Heteromeric Kv2 channels in mammalian brain neurons. J. Biol. Chem 285, 15048–15055. [PubMed: 20202934]

Kirmiz M, et al., 2018 Remodeling neuronal ER-PM junctions is a conserved non-conducting function of Kv2 plasma membrane ion channels. Mol. Biol. Cell 29, 2410–2432. [PubMed: 30091655]

Kuang Q, et al., 2015 Structure of potassium channels. Cell. Mol. Life Sci 72, 3677–3693. [PubMed: 26070303]

Latypova X, et al., 2017 Novel KCNB1 mutation associated with non-syndromic intellectual disability. J. Hum. Genet 62, 569–573. [PubMed: 27928161]

Lim ST, et al., 2000 A novel targeting signal for proximal clustering of the Kv2.1 K+ channel in hippocampal neurons. Neuron 25, 385–397. [PubMed: 10719893]

Liu PW, Bean BP, 2014 Kv2 channel regulation of action potential repolarization and firing patterns in superior cervical ganglion neurons and hippocampal CA1 pyramidal neurons. J. Neurosci 34, 4991–5002. [PubMed: 24695716]

Mandikian D, et al., 2014 Cell type-specific spatial and functional coupling between mammalian brain Kv2.1 K+ channels and ryanodine receptors. J. Comp. Neurol 522, 3555–3574. [PubMed: 24962901]

Marini C, et al., 2017 Clinical features and outcome of 6 new patients carrying de novo KCNB1 gene mutations. Neurol Genet. 3, e206. [PubMed: 29264397]

Matsuoka Y, et al., 2005 Prostaglandin E receptor EP1 controls impulsive behavior under stress. Proc. Natl. Acad. Sci. U. S. A 102, 16066–16071. [PubMed: 16247016]

McTague A, et al., 2016 The genetic landscape of the epileptic encephalopathies of infancy and childhood. Lancet Neurol. 15, 304–316. [PubMed: 26597089]

Miao P, et al., 2017 A novel mutation in KCNB1 gene in a child with neuropsychiatric comorbidities with both intellectual disability and epilepsy and review of literature. Zhonghua Er Ke Za Zhi. 55, 115–119. [PubMed: 28173649]

Misonou H, et al., 2004 Regulation of ion channel localization and phosphorylation by neuronal activity. Nat. Neurosci 7, 711–718. [PubMed: 15195093]

Mohapatra DP, Trimmer JS, 2006 The Kv2.1 C terminus can autonomously transfer Kv2.1-like phosphorylation-dependent localization, voltage-dependent gating, and muscarinic modulation to diverse Kv channels. J. Neurosci 26, 685–695. [PubMed: 16407566]

Murakoshi H, Trimmer JS, 1999 Identification of the Kv2.1 K+ channel as a major component of the delayed rectifier K+ current in rat hippocampal neurons. J. Neurosci 19, 1728–1735. [PubMed: 10024359]

Murakoshi H, et al., 1997 Phosphorylation of the Kv2.1 K+ channel alters voltage-dependent activation. Mol. Pharmacol 52, 821–828. [PubMed: 9351973]

O'Connell KM, et al., 2008 Localization and mobility of the delayed-rectifer K+ channel Kv2.1 in adult cardiomyocytes. Am. J. Physiol. Heart Circ. Physiol 294, H229–H237. [PubMed: 17965280]

Palacio S, et al., 2017 Heterogeneity in Kv2 channel expression shapes action potential characteristics and firing patterns in CA1 versus CA2 hippocampal pyramidal neurons. ENEURO 4 (ENEURO.0267–17.2017).

Peltola MA, et al., 2011 AMIGO is an auxiliary subunit of the Kv2.1 potassium channel. EMBO Rep. 12, 1293–1299. [PubMed: 22056818]

Rasband WS, 1997–2018 ImageJ. U. S. National Institutes of Health, Bethesda, Maryland, USA.

Rhodes TH, et al., 2004 Noninactivating voltage-gated sodium channels in severe myoclonic epilepsy of infancy. Proc. Natl. Acad. Sci. U. S. A 101, 11147–11152. [PubMed: 15263074]

Saitsu H, et al., 2015 De novo KCNB1 mutations in infantile epilepsy inhibit repetitive neuronal firing. Sci. Rep 5, 15199. [PubMed: 26477325]

Sarmiere PD, et al., 2008 The Kv2.1 K+ channel targets to the axon initial segment of hippocampal and cortical neurons in culture and in situ. BMC Neurosci. 9, 112. [PubMed: 19014551]

Scannevin RH, et al., 1996 Identification of a cytoplasmic domain important in the polarized expression and clustering of the Kv2.1 K+ channel. J. Cell Biol 135, 1619–1632. [PubMed: 8978827]

Scheffer IE, et al., 2017 ILAE classification of the epilepsies: position paper of the ILAE Commission for classification and terminology. Epilepsia 58, 512–521. [PubMed: 28276062]

Shaw G, et al., 2002 Preferential transformation of human neuronal cells by human adenoviruses and the origin of HEK 293 cells. FASEB J. 16, 869–871. [PubMed: 11967234]

Shepherd JK, et al., 1994 Behavioural and pharmacological characterisation of the elevated "zero-maze" as an animal model of anxiety. Psychopharmacology 116, 56–64. [PubMed: 7862931]

Shi G, et al., 1994 Properties of Kv2.1 K+ channels expressed in transfected mammalian cells. J. Biol. Chem 269, 23204–23211. [PubMed: 8083226]

Speca DJ, et al., 2014 Deletion of the Kv2.1 delayed rectifier potassium channel leads to neuronal and behavioral hyperexcitability. Genes Brain Behav. 13, 394–408. [PubMed: 24494598]

Srivastava S, et al., 2018 Monogenic disorders that mimic the phenotype of Rett syndrome. Neurogenetics 19, 41–47. [PubMed: 29322350]

Thiffault I, et al., 2015 A novel epileptic encephalopathy mutation in KCNB1 disrupts Kv2.1 ion selectivity, expression, and localization. J. Gen. Physiol 146, 399–410. [PubMed: 26503721]

Torkamani A, et al., 2014 De novo KCNB1 mutations in epileptic encephalopathy. Ann. Neurol 76, 529–540. [PubMed: 25164438]

Trimmer JS, 1991 Immunological identification and characterization of a delayed rectifier K+ channel polypeptide in rat brain. Proc. Natl. Acad. Sci 88, 10764–10768. [PubMed: 1961744]

Electrical stimulation seizure models In: van Vliet EA, Gorter JA, Pitkanen A, Buckmaster PS, Galanopoulou AS, Moshe SL (Eds.), 2017 Models of Seizures and Epilepsy. Elsevier Inc., Boston, pp. 474–488.

Vierra NC, et al., 2019 Kv2.1 mediates spatial and functional coupling of L-type calcium channels and ryanodine receptors in mammalian neurons. Elife 8.

Wu Y, et al., 2017 Contacts between the endoplasmic reticulum and other membranes in neurons. Proc. Natl. Acad. Sci 114, E4859–E4867. [PubMed: 28559323]

Yamashita M, et al., 2013 Impaired cliff avoidance reaction in dopamine transporter knockout mice. Psychopharmacology 227, 741–749. [PubMed: 23397052]

Yu SP, Kerchner GA, 1998 Endogenous voltage-gated potassium channels in human embryonic kidney (HEK293) cells. J. Neurosci. Res 52, 612–617. [PubMed: 9632317]

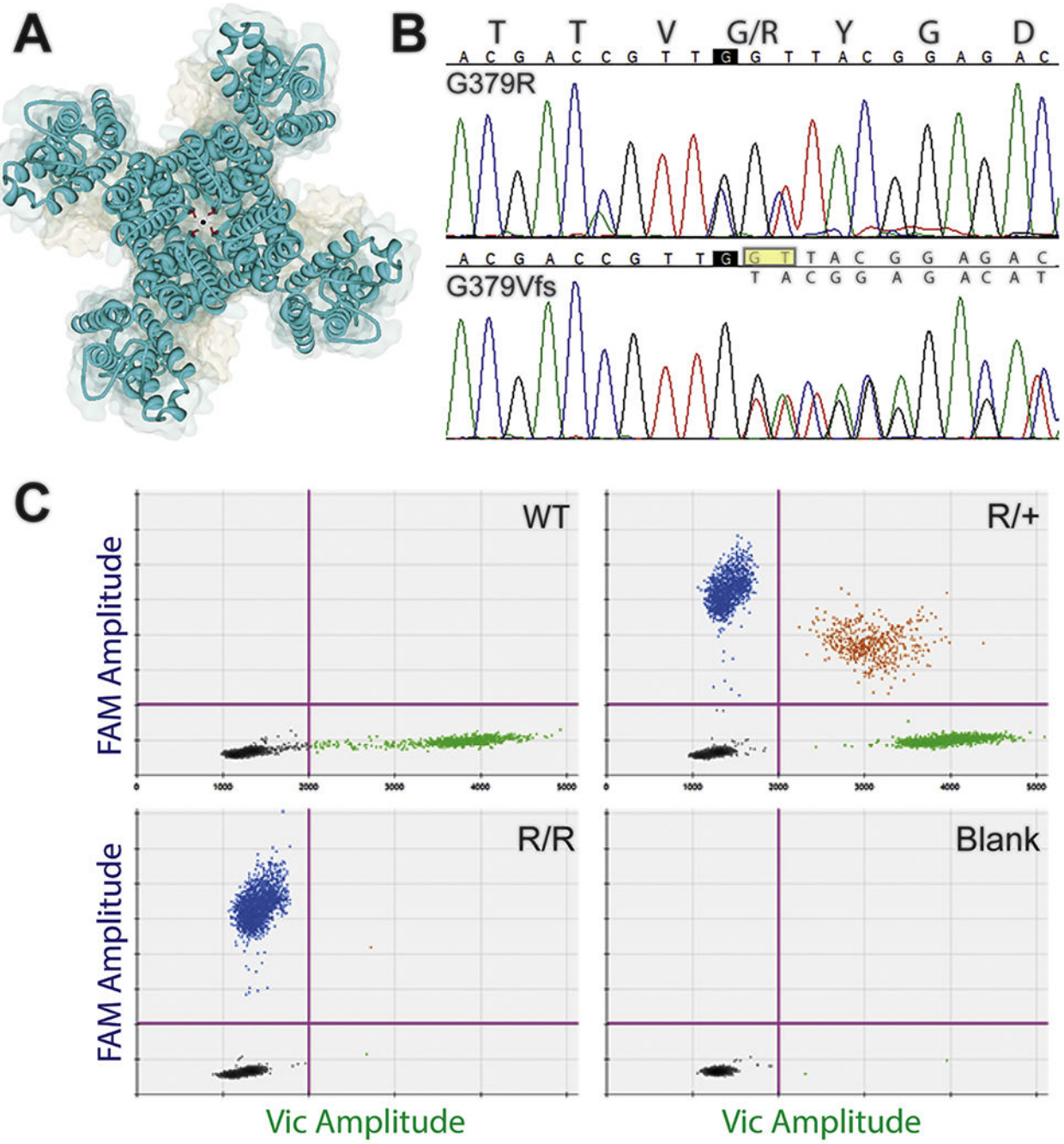

Fig. 1.

Generation and molecular characterization of *Kcnb1*^{G379R} Mice. A) Location of glycine-379 in the K_v2.1 tetrameric potassium channel subunit (PDB 29R9 K_v2.1/K_v1.2 chimera). G379 (red) is one of the critical 'GYG' residues that determines potassium selectivity and resides in the central pore where backbone carbonyls coordinate the K^+ ions as they traverse the selectivity filter (black circle). B) Sequencing chromatograms of *Kcnb1* genomic PCR products with the first nucleotide of the G379 codon highlighted in black. Top chromatogram was from a heterozygous *Kcnb1*$^{R/+}$ mouse (G379R) showing heterozygosity

for the 3 nucleotides changes introduced by CRISPR/Cas9 editing and homology directed repair. Two nucleotide changes in codon 379 resulted in substitution of arginine for glycine, and a silent substitution in codon 377 disrupted an adjacent PAM site. Bottom chromatogram was from a heterozygous *Kcnb1*$^{fs/+}$ mouse (G379Vfs) showing the 2 nucleotide deletion (yellow highlighted box) introduced by CRISPR/Cas9 editing and non-homologous end joining. This resulted in the frameshift G379VfsTer6. C) Multiplex ddPCR-based genotyping using hydrolysis probes for the WT and G379R alleles distinguishes between the three possible genotypes, WT, *Kcnb1*$^{R/+}$ and *Kcnb1*$^{R/R}$. Representative two-dimensional scatterplots of each genotype are shown along with a no template control (blank). Each scatterplot represents >10,000 partitioned reactions. Within a scatterplot, each point represents a droplet with a given fluorescence level and droplet colors indicate target amplification about threshold (magenta lines). Droplet colour code: green = positive for WT; blue = positive for G379R; orange = positive for both; black = negative.

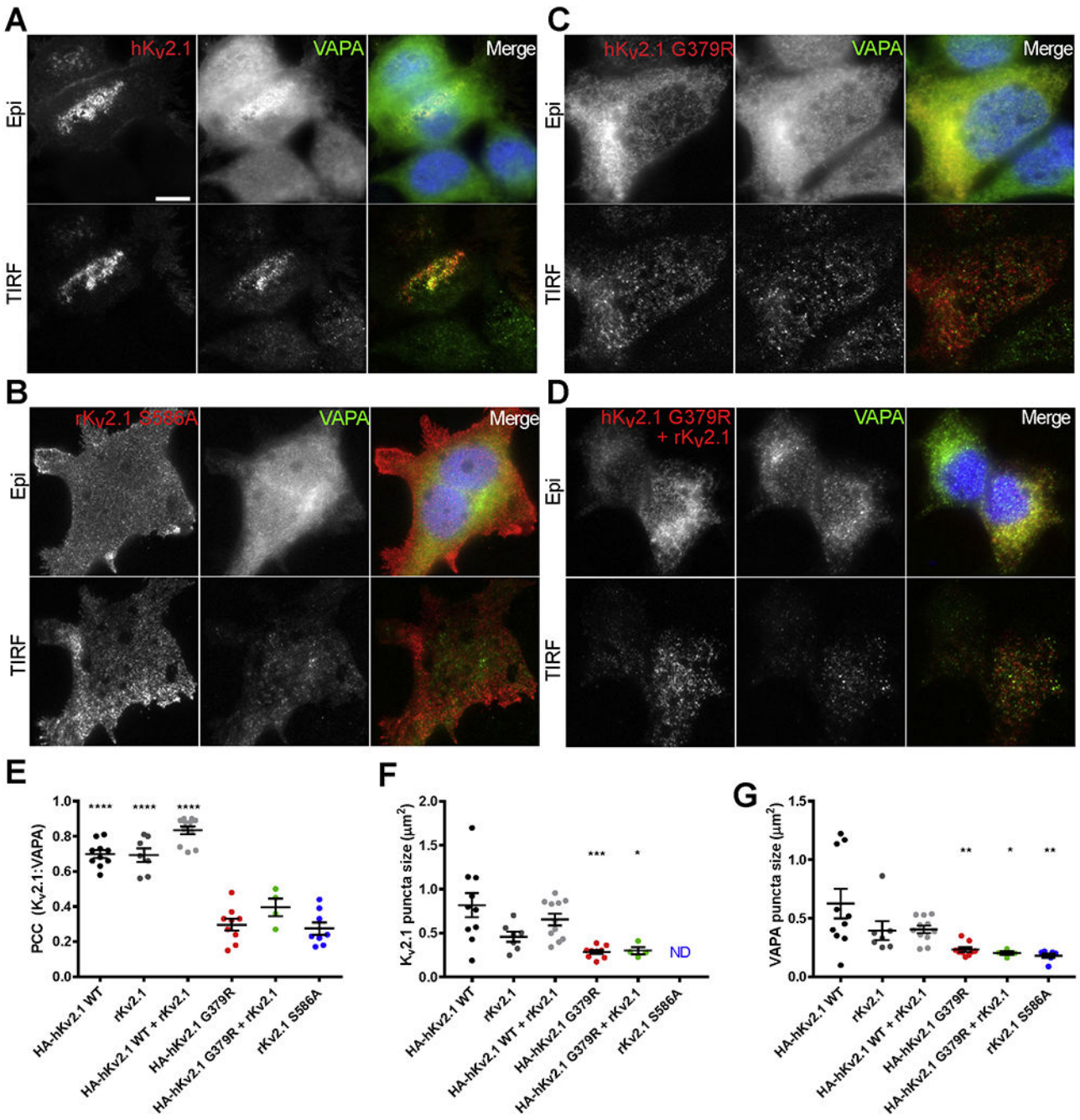

Fig. 2.

G379R mutation disrupts K_v2.1-mediated recruitment of VAPA to ER-PM junctions in HEK293T cells. A–D) Representative wide-field epifluorescence ("Epi") and TIRF images of HEK293T cells expressing hK_v2.1 WT (A), rK_v2.1 S586A (B), hK_v2.1 G379R (C) and hK_v2.1 G379R + rK_v2.1 (D). Red- K_v2.1, Green- VAPA and Blue- Hoechst. Scale bar = 10 μm. E) Scatter plot of Pearson's correlation Coefficient (PCC) values for colocalization of K_v2.1 and VAPA for each transfection condition. PCC values were higher for hK_v2.1 WT (0.699 ± 0.02), rK_v2.1 (0.69 ± 0.04), and hK_v2.1 WT + rK_v2.1 (0.84 ± 0.02) compared to

rK$_v$2.1 S586A (0.28 ± 0.04), hK$_v$2.1 G379R (0.3 ± 0.03), and hK$_v$2.1 G379R + rK$_v$2.1 (0.4 ± 0.05) ($F(5,43) = 62.453$, $p < 0.0001$; one-way ANOVA; n = 4–12 cells). ****p < 0.0001. F) Scatter plot of K$_v$2.1 puncta size for each transfection condition. hK$_v$2.1 G379R (0.284 ± 0.2 μm^2) and hK$_v$2.1 G379R + rK$_v$2.1 (0.34 ± 0.4 μm^2) had smaller K$_v$2.1 puncta size compared to hK$_v$2.1 WT (0.82 ± 0.14 μm^2) ($F(4,36) = 6.763$, $p = 0.0004$; one-way ANOVA; n = 4–12 cells). ND: Not determined, p = ***0.0006, *p = 0.0130. G) Scatter plot of VAPA puncta size for each transfection condition. hK$_v$2.1 G379R (0.23 ± 0.02 μm^2), hK$_v$2.1 G379R T rK$_v$2.1 (0.20 ± 0.02 μm^2) and rK$_v$2.1 S586A (0.181 ± 0.02 μm^2) had smaller VAPA puncta size compared to hK$_v$2.1 WT (0.63 ± 0.13 μm^2) ($F(5,42) = 5.39$, $p = 0.0006$; one-way ANOVA). n = 4–12 cells. **p = 0.0028, *p = 0.0181, **p = 0.0014. Error bars represent SEM.

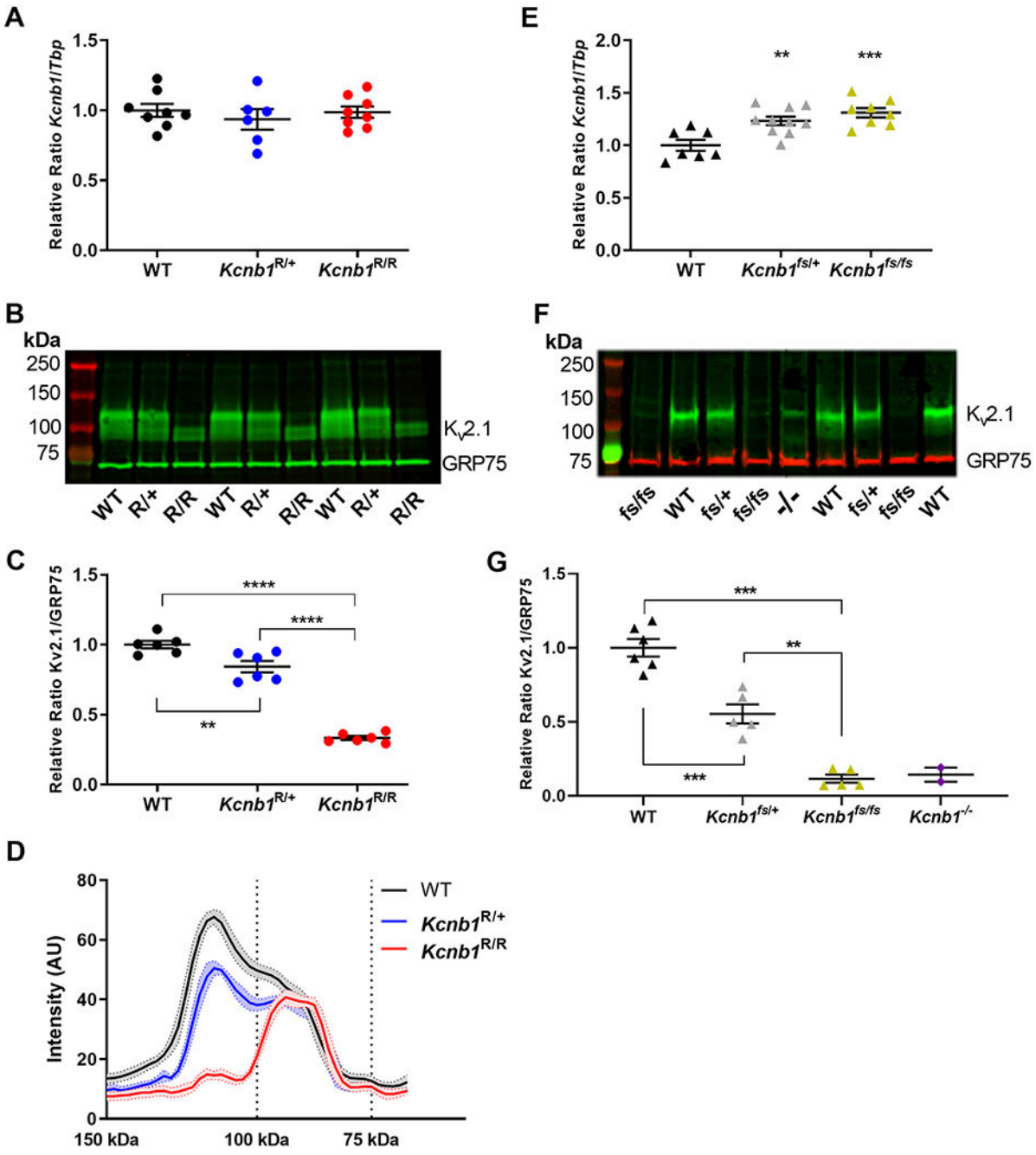

Fig. 3.

Expression of *Kcnb1* transcript and $K_v2.1$ protein in *Kcnb1*^{G379R} and *Kcnb1*^{fs} mice. A) Relative expression of whole brain *Kcnb1* transcript in WT, *Kcnb1*$^{R/+}$ and *Kcnb1*$^{R/R}$ assayed by quantitative RT-ddPCR. There was no difference in transcript expression between genotypes ($F(2,19) = 0.3806$, $p > 0.68$; one-way ANOVA; n = 6–8 mice per genotype). B) Representative $K_v2.1$ immunoblot of *Kcnb1*^{G379R} brain membrane protein using the anti-$K_v2.1$ K89/34 mAb. The anti-GRP75 mAb is used as a loading control. C) Quantification of the $K_v2.1$/GRP75 ratio on immunoblots showed ≈15% lower $K_v2.1$ expression in *Kcnb1*$^{R/+}$

and ≈67% lower in *Kcnb1*$^{R/R}$ relative to WT ($F(2,15) = 139.9$, $p < 0.0001$; one-way ANOVA; n = 6 mice per genotype; **p = 0.0049, ****p < 0.0001). D) Line scan analysis of immunoblots showing a genotype-dependent shift in post-translational modification state of $K_v2.1$ from a heterogeneous pool (M_r ≈ 100–130 kDa) in WT and *Kcnb1*$^{R/+}$ samples to an M_r more closely approximating the predicted molecular weight of 95 kDa in *Kcnb1*$^{R/R}$ samples. Lines are the average of 6 samples per genotype and SEM is represented by the shading. E) Relative expression of whole brain *Kcnb1* transcript in WT, *Kcnb1*$^{fs/+}$ and *Kcnb1*$^{fs/fs}$ assayed by quantitative RT-ddPCR. There was a modest elevation of *Kcnb1* transcript expression compared to WT ($F(2,22) = 11.48$, $p = 0.0004$; one-way ANOVA; n = 7–10 mice per genotype; **p = 0.004, ***p = 0.0004). F) Representative $K_v2.1$ immunoblot of *Kcnb1*^{fs} brain membrane protein using the anti-$K_v2.1$ K39/25 mAb. The anti-GRP75 mAb is used as a loading control. G) Quantification of the $K_v2.1$/GRP75 ratio on immunoblots showed ≈45% lower $K_v2.1$ expression in *Kcnb1*$^{fs/+}$ and ≈89% lower in *Kcnb1*$^{fs/fs}$ relative to WT littermates. *Kcnb1*$^{-/-}$ control sample (purple circles) had similar expression of ≈85% compared to WT, suggesting that residual signal is non-specific and *KcnbP*^{fs} line is comparable to a knockout ($F(2,13) = 68.6$, $p < 0.0001$; n = 2–6 mice per genotype; **p = 0.0003, ***p < 0.0002). For panels A, C, E and G, symbols represent samples from individual mice and error bars represent SEM.

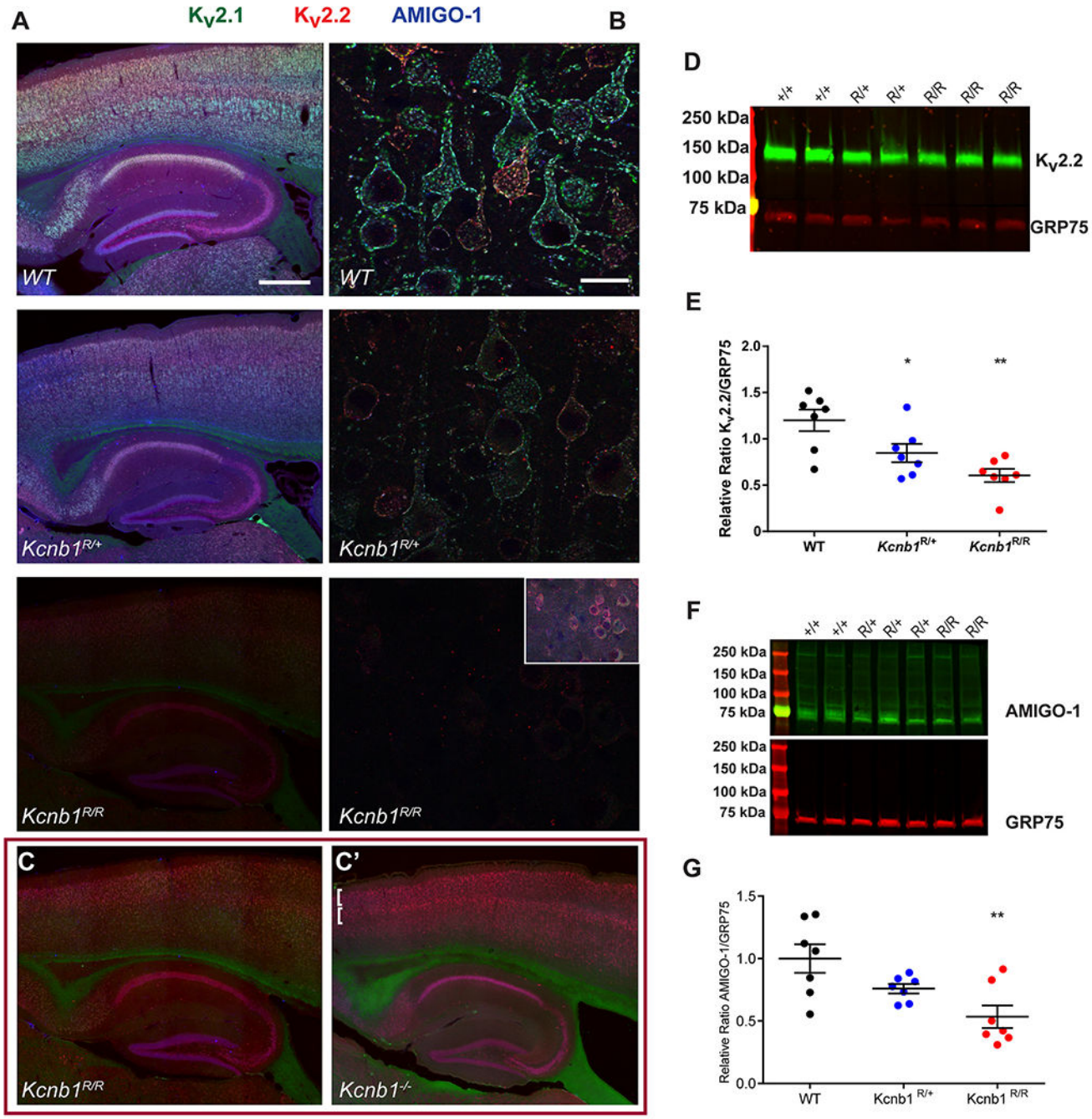

Fig. 4.

Immunolabeling of K_V2 channel complexes in *Kcnb1*^{G379R} brain sections and membrane preps. A) Representative images of somatosensoiy cortex and hippocampus from littermate WT, *Kcnb1*$^{R/+}$ and *Kcnb1*$^{R/R}$ mice. Signal intensities for $K_V2.1$ (green), $K_V2.2$ (red), and AMIGO-1 (blue) immunolabeling are lower in *Kcnb1*$^{R/R}$ mice. Scale bar = 50 μm. B) Representative high magnification images of layer 5b of somatosensory cortex from littermate WT, *Kcnb1*$^{R/+}$ and *Kcnb1*$^{R/R}$ mice. Inset panel is 3x size reduced image with enhanced signal intensity to show that the immunolabeling remaining in the sample from the

Kcnb1$^{R/R}$ mouse appears to be primarily intracellular compared to WT and *Kcnb1*$^{R/+}$ mice. Scale bar = 20 μm. C) Image of bottom left panel of A with enhanced signal intensity, showing that the remaining signal is predominantly K_v2.2 (red) and to a lesser extent AMIGO-1 (blue). CO Representative image of somatosensoiy cortex and hippocampus from *Kcnb1*$^{-/-}$ at the same exposure as panels A and B showing a pattern of immunolabeling similar to the pattern observed in the *Kcnb1*$^{R/R}$ section after enhancement of signal intensity as shown in panel C. D) Representative K_v2.2 immunoblot. The anti-GRP75 mAb is used as a loading control. E) Quantification of the Kv2.2/GRP75 ratio on immunoblots showed ≈30% lower expression in *Kcnb1*$^{R/+}$ and ≈50% lower in *Kcnb1*$^{R/R}$ relative to WT ($F(2,18) = 9.525$, $p = 0.0015$; one-way ANOVA; n = 7 mice per genotype; *$p < 0.05$, **$p < 0.002$). F) Representative AMIGO-1 immunoblot. The anti-GRP75 mAb is used as a loading control. G) Quantification of AMIGO-1/GRP75 ratio on immunoblots showed ≈25% lower expression in *Kcnb1*$^{R/+}$ and ≈47% lower in *Kcnb1*$^{R/R}$ relative to WT ($F(2,18) = 7.168$, $p = 0.0051$; one-way ANOVA; n = 7 mice per genotype; **$p < 0.004$). For panels E and G, symbols represent samples from individual mice and error bars represent SEM.

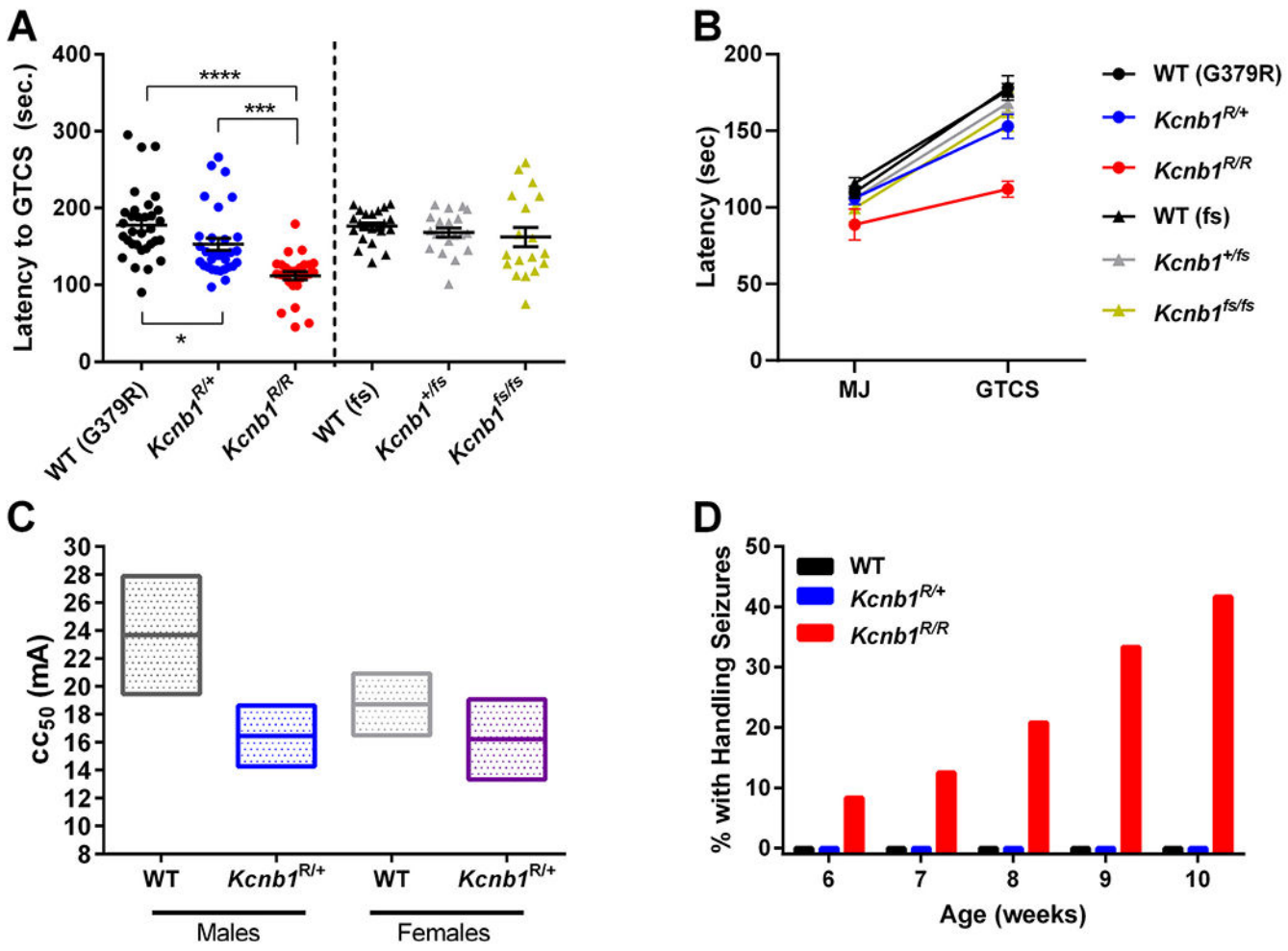

Fig. 5.

Kcnb1$^{R/+}$ and *Kcnb1*$^{R/R}$ mice are sensitive to induced seizures. A) Latency to flurothyl-induced GTCS was affected by *Kcnb1*^{G379R} genotype (H(2) = 38.92, p < 0.0001, Kruskal-Wallis; n = 28–32 mice per genotype). *Kcnb1*$^{R/+}$ mice had a reduced seizure threshold of 153 ± 8 s compared to WT with an average latency of 178 ± 8s. *Kcnb1*$^{R/R}$ mice had the shortest average latency of 112 — 5 s, which was lower than WT or *Kcnb1*$^{fs/fs}$. There were no differences in GTCS latency between WT, *Kcnb1*$^{fs/+}$ or *Kcnb1*$^{fs/fs}$ mice (F(2,57) = 0.8234, p = 0.44; n = 18–22 mice per genotype). Symbols represent individual mice and error bars represent SEM. *p = 0.0412, ***p = 0.0005, ****p < 0.0001 B) Average latencies to first myoclonic jerk (MJ) and GTCS are shown, with the connecting line depicting time of progression between the stages. Although there was no difference in MJ latency for *Kcnb1*^{G379R} versus WT mice, progression between the stages was faster for *Kcnb1*$^{R/R}$ and *Kcnb1*$^{R/+}$ mice relative to WT (p = 0.0040, p = 0.0438, respectively; Dunn's). There were no differences in average latencies or progression time between the stages for *Kcnb1*$^{fs/+}$, *Kcnb1*$^{fs/fs}$ and WT mice (Table 3). C) Susceptibility to psychomotor seizures induced by 6 Hz stimulation. *Kcnb1*$^{R/+}$ mice had lower CC_{50} values (convulsive current, 50% with seizures) compared to WT (p < 0.0001, log-probit). The CC_{50} values (95% confidence interval) for male WT and *Kcnb1*$^{R/+}$ mice were 23.7 mA (19.5 to 27.9) and 16.4 mA (14.3

to 18.6), respectively. The CC_{50} values for female WT and *Kcnb1*$^{R/+}$ mice were 18.7 mA (16.5 to 20.9) and 16.2 mA (13.3 to 19.1), respectively. Floating box graph represents 95% Cl and CC_{50} (line). CC_{50} and CI were determined using log-probit analysis with n = 2–20 per current. D) Handling-induced seizures were observed in *Kcnb1*$^{R/R}$ mice at 6–12 weeks of age, while they were not observed in *Kcnb1*$^{R/+}$ or WT mice in this age window ($p < 0.001$, n = 23–24 mice per genotype). Rare handling-induced seizures were observed in *Kcnb1*$^{R/+}$ mice at >4 months of age.

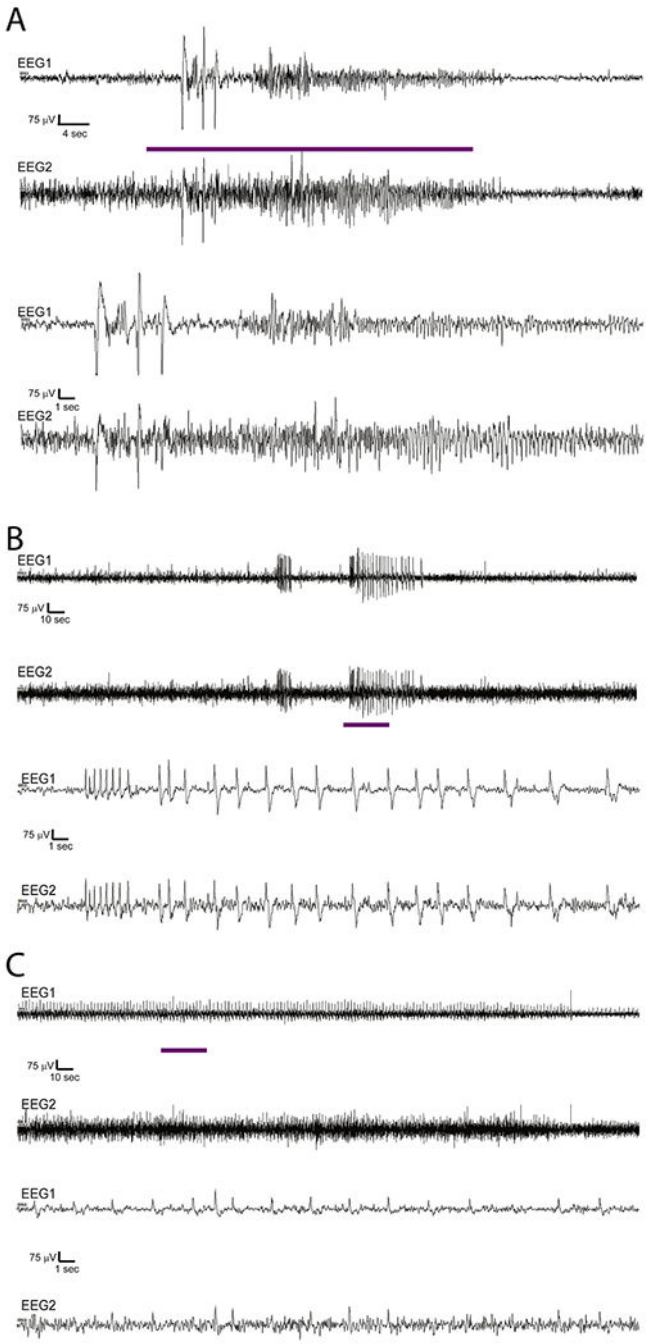

Fig. 6.

Ictal EEG abnormalities in *Kcnb1*^{G379R} mice. A) Representative EEG traces from *Kcnb1*$^{R/R}$ mouse exhibiting a spontaneous tonic-clonic seizure (see Supplemental Video S2 and S2a for the corresponding videos). The top line corresponds to EEG1 (right poster-left posterior) and the second line corresponds to EEG2 (right anterior to left posterior) in each set of traces. The upper two traces display 2 min of EEG and the purple line denotes the one minute expanded in the lower two traces. The scale bar for the 2-min time base are 75 μV and 4 s and the scale bar for the 1-min time base are 75 μV and 1 s. B-C) Representative

EEG traces from a *Kcnb1*$^{R/R}$ mouse with repetitive runs of slow spike-wave discharges. The top line corresponds to EEG1 and the second line corresponds to EEG2. The top two lines display 5 min of EEG and the purple line denotes the 30 s region of expanded time base displayed below. The scale bar for the 5-min time base are 75 μV and 10 s and the scale bar for the 30 s segment are 75 μV and 1 s, respectively. Neither of these runs had apparent clinical correlate with B occurring during wakefulness while the animal was moving around the cage and C occurring during a 15-min run of discharges during sleep.

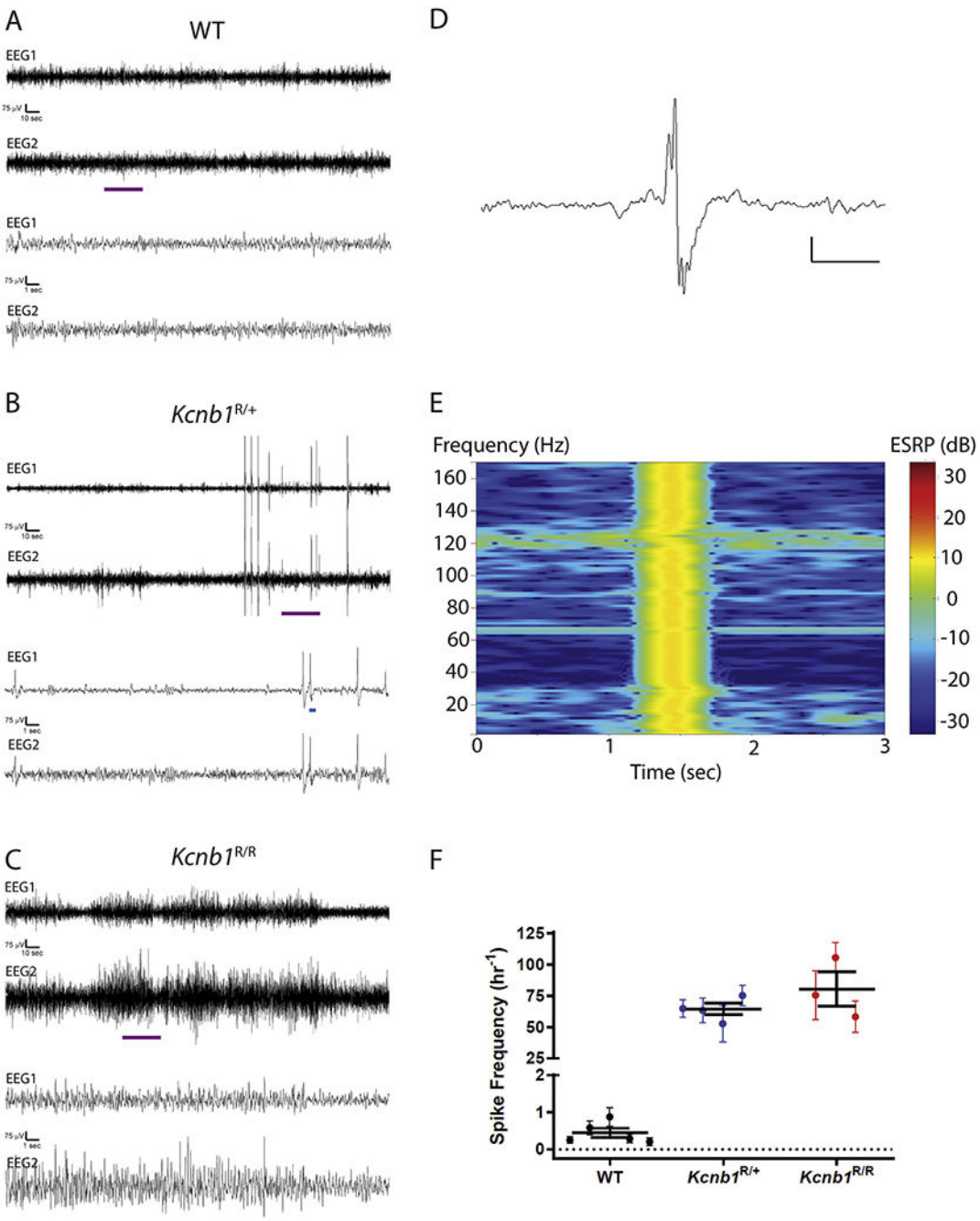

Fig. 7.

Interietal EEG abnormalities in *Kcnb1*^{G379R} mice. A–C) Representative EEG traces from WT, *Kcnb1*$^{R/+}$, and *Kcnb1*$^{R/R}$ mice. The top line corresponds to EEG1 (right posterior-left posterior) and the second line corresponds to EEG2 (right anterior to left posterior) in each set of traces. The top two lines display 5 min of EEG and the purple line denotes the 30 s region of expanded time base displayed below. The scale bar for the 5-min time base are 75 μV and 10 s and the scale bar for the 30 s segment are 75 μV and 1 s, respectively. D) Example isolated spike and slow wave discharge corresponding to blue line in B. E) Power

spectrum for spike and slow wave discharge in D showing elevated power in decibels across the 1–170 Hz frequency range at the time of the discharge. F) Quantification of isolated spike and slow wave discharges for each genotype (WT n = 5; *Kcnb1*$^{R/+}$ n = 4; *Kcnb1*$^{R/R}$ n = 3) over a 24-h period and displayed as frequency per hour. Symbols represent the mean for an individual animal ± SEM. Horizontal lines represent the mean ± SEM for all animals of that genotype.

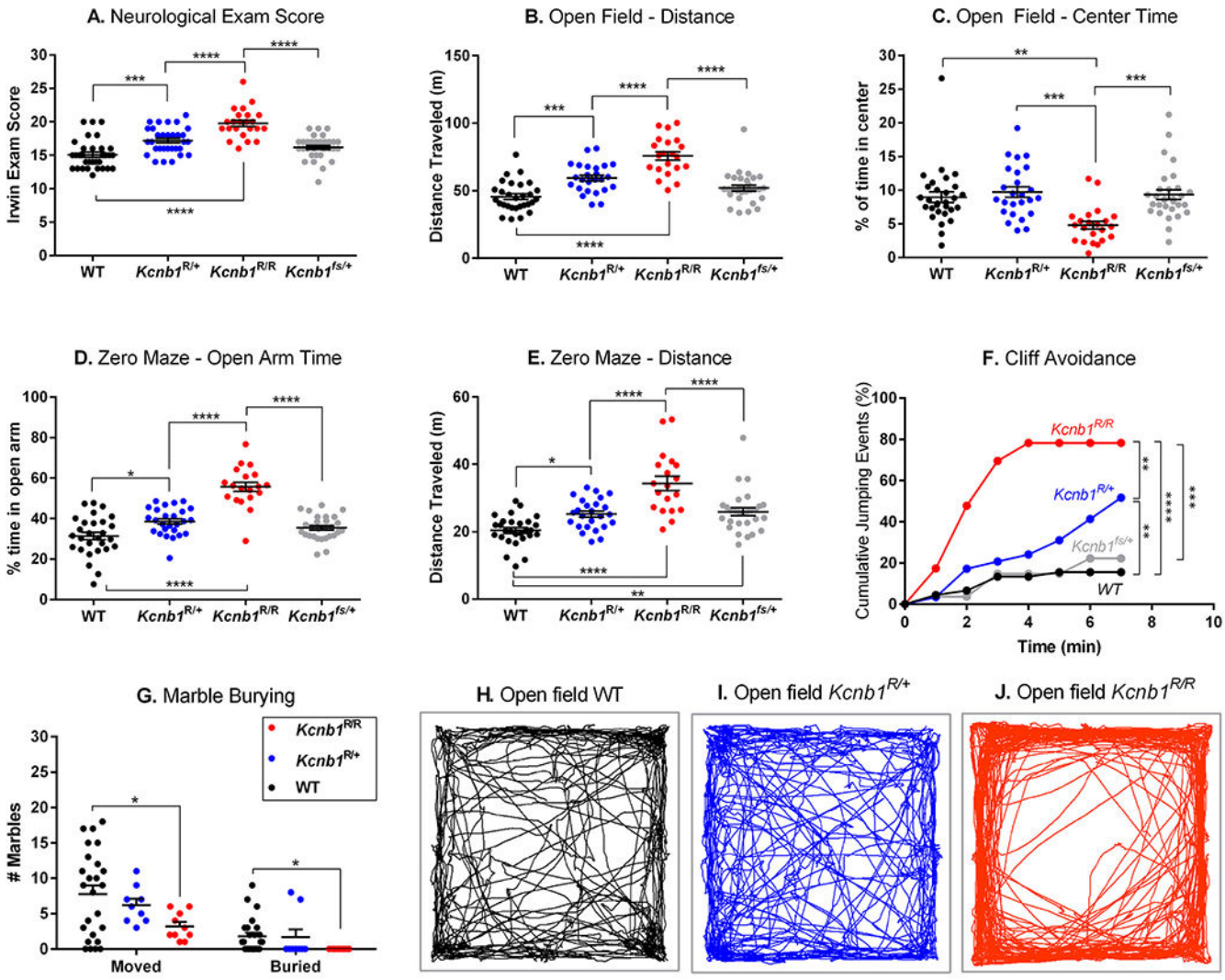

Fig. 8.

Neurological and neurobehavioral phenotypes in *Kcnb1*^{G379R} and *Kcnb1*$^{fs/+}$ mice. A) Modified Irwin neurological exam scores were affected by genotype (F (3,114) = 25.82, p < 0.0001; one-way ANOVA). *Kcnb1*$^{R/+}$ mice had an average score of 17.2 ± 0.4, higher compared to the WT score of 15.1 ± 0.4. *Kcnb1*$^{R/R}$ mice had the highest score, with an average score of 19.8 ± 0.5. *Kcnb1*$^{fs/+}$ mice had an average score of 16.2 ± 0.3 (n = 23–32 mice per genotype; ***p = 0.0004, ****p < 0.0001). B) Distance traveled in an open field assay was affected by genotype (F(3,100) = 28.31, p < 0.0001; one-way ANOVA). *Kcnb1*$^{R/+}$ mice traveled an average distance of 59.3 ± 2.2 m, farther compared to WT average distance of 45.6 ± 2.0 m. *Kcnb1*$^{R/R}$ mice traveled an average distance of 75.8 ± 3.1 m, farther than both WT and *Kcnb1*$^{R/+}$ mice. *Kcnb1*$^{fs/+}$ mice traveled an average distance of 52.0 ± 2.2 m (n = 21–29 mice per genotype; ***p = 0.0003, ****p < 0.0001). C) There was a significant effect of genotype on percent of time spent in the center of the open field (F(3,102) = 8.435, p < 0.0001; one-way ANOVA). *Kcnb1*$^{R/R}$ mice spent 4.8 ± 0.6% of time in the center, less than WT, *Kcnb1*$^{R/+}$ and *Kcnb1*$^{fs/+}$ mice (n = 22–30 mice per genotype; **p = 0.0011, ***p < 0.0004). D) Time spent in the open arms of the zero-maze was affected by genotype

(F(3,97) = 35.51, p < 0.0001; one-way ANOVA). *Kcnb1*$^{R/+}$ mice averaged 38.6 ± 1.3% of the test time in open arms of the maze compared to WT mice that averaged 31.4 ± 1.9% of time. *Kcnb1*$^{R/R}$ mice spent 55.7 ± 2.3% of time in the open arms of the maze, more than WT, *Kcnb1*$^{R/+}$ and *Kcnb1*$^{fs/+}$ (35.4 ± 1.1%) mice (n = 19–28 mice per genotype; *p = 0.01, ****p < 0.0001). E) There was a significant effect of genotype on total distance traveled in the zero maze (F(3,96) = 19.96, p < 0.0001; one-way ANOVA). *Kcnb1*$^{R/R}$ mice traveled the farthest distance of 34.3 ± 2.1 m compared to 25.2 ± 0.9 m for *Kcnb1*$^{R/+}$, 26.0 ±1.2 for *Kcnb1*$^{fs/+}$ and 20.4 ± 0.8 m for WT (n = 19–28 mice per genotype; *p = 0.0236, **p = 0.005, ****p < 0.0001). F) Time to step or jump off an elevated platform was evaluated in the cliff avoidance assay. *Kcnb1*$^{R/+}$ mice left the platform more frequently (≈52%, 15/29) compared to WT (≈15%, 4/26). Approximately 78% of *Kcnb1*$^{R/R}$ mice (18/23) left the platform, more than WT, *Kcnb1*$^{R/+}$ and *Kcnb1*$^{fs/+}$ (≈22%, 3/15) mice. **p < 0.009, ***p < 0.0007, ****p < 0.0001. G) Marble burying was significantly affected by genotype. (F(2,41) = 3.518, p = 0.0389; two-way repeated measures ANOVA). Relative to WT, *Kcnb1*$^{R/+}$ mice rarely and *Kcnb1*$^{R/R}$ mice never buried marbles (n = 9–25 mice per genotype; *p = 0.0225). H-J) Representative examples of movement paths in the open-field assay for WT, *Kcnb1*$^{R/+}$ and *Kcnb1*$^{R/R}$ mice. For panels A-E and G, symbols represent individual mice, horizontal lines represent mean and error bars represent SEM.

Table 1

List of primers and probes.

Assay	Description	Sequence
Founder Screening PCR	Primer 1	5′-TGGGCTTGCTCATCCTCTTC
	Primer 2	5′-CTCCGCTTGATGGCTTTCTC
Genotyping *Kcnb1*^{G379R}	Primer 1	5′-GCATCCCCGCCTCTTTCT
	Primer 2	5′-CAGGAGAGTCTTAGGGTAGATGTCT
	Probe 1 (WT allele)	5′-VIC-CACCATGACGACCGTT-NFQ
	Probe 2 (mutant allele)	5′-FAM-CACCATGACGACAGTT-NFQ
Genotyping *Kcnb1*^{fs}	Primer 1	5′-TCTTTGCCGAGAAGGATGAG
	Primer 2	5′-CCAGGAGAGTCTTAGGGTAGAT
	Probe 1 (common allele)	5′-VIC-TAGCCCACCAGAAAGAGGC-NFQ
	Probe 2 (WT allele)	5′-FAM-ATGACGACCGTTGGTTACGG-NFQ

Abbreviations: FAM, FAM reporter dye; VIC, VIC reporter dye; NFQ, nonfluorescent quencher.

Neurobiol Dis. Author manuscript; available in PMC 2021 January 01.

Table 2

List of antibodies.

Antibody (target)	Immunogen	Manufacturer information	Concentration/dilution used	Figures
12CA5 (HA epitope)	Influenza hemagglutinin HA epitope tag	Mouse IgG2b mAb, In-house (Trimmer Laboratory) RRID:AB_2532070	Pure, 5 μg/mL	2
N479/24 (VAPA)	Fusion protein aa 1–219 of rat VAPA	Mouse IgG2a mAb, In-house (Trimmer Laboratory) RRID:AB_2722709	Tissue culture supernatant, 1:5	2
N52A/42 GRP75/mortalin)	Identified as off-target mAb in screen for anti-SALM2 mAbs	Mouse IgG1 mAb, NeuroMab RRID:AB_2120479	Pure, 1 μg/mL	3, 4
K89/34 (K_v2.1)	Synthetic peptide aa 837–853 of rat K_v2.1	Mouse IgG1 mAb, NeuroMab RRID:AB_RRID:10673392	Pure, 2–5 μg/mL	3,4, S3
K39/25 (K_v2.1)	Synthetic peptide aa 211–220 of human K_v2.1	Mouse IgG2a mAb, NeuroMab RRID:AB:2131649	Pure, 10 μg/mL	3
L86/33 (AMIGO-1)	Fusion protein aa 394-492 of mouse AMIGO-1	Mouse IgG2a mAb, Neuro Mab RRID:AB_2315798	Tissue culture supernatant, 1:5	3,4
Kv2.2C (K_v2.2)	Fusion protein aa 717–907 of rat K_v2.2 long isoform	Rabbit pAb, In-house (Trimmer Laboratory), RRID:AB_2801484	Affinity purified, 1:100	3,4
ab32454 (MAP2)	Synthetic peptide within Rat MAP2 aa 1–100 (N terminal)	Rabbit pAb, Abeam RRID:AB_776174	Affinity purified 1:1000	S3
D3/71R (K_v2.1)	Fusion protein aa 506-533 of rat K_v2.1	Mouse IgG2a recombinant mAb, In-house (Trimmer Laboratory) RRID: AB_2750651	Tissue culture supernatant, 1:5	S4
L80/21 (K_v2.1)	Synthetic peptide aa 837-853 of rat K_v2.1	Mouse IgG3 mAb, Neuro Mab RRID:AB_2315862	Tissue culture supernatant, 1:5	S4
L105/31 (K_v2.1)	Synthetic peptide aa 596-616 of rat K_v2.1	Mouse IgG1 mAb, In-house (Trimmer Laboratory) RRID:AB_2801485	Tissue culture supernatant, 1:5	S4
L114/3 (Parvalbumin)	Fusion protein amino acids 1–110 of rat Parvalbumin	Mouse IgG2a mAb, NeuroMab RRID:AB_2629420	Tissue culture supernatant, 1:5	S4
L122/6 (Calretinin)	Fusion protein amino acids 1–178 of human Calretinin	Mouse IgG2b mAb, NeuroMab RRID:AB _2716256	Tissue culture supernatant, 1:5	S4

Table 3

Statistical comparisons.

Figure	Comparison	Test	Value	Post hoc
2E	PCC (K_v2.1:VAPA)	One-way ANOVA	F(5,43) = 62.453, p < 0.0001	Tukey
2F	K_v2.1 Puncta Size	One-way ANOVA	F(4,36) = 6.763, p = 0.0004	Tukey
2G	VAPA Puncta Size	One-way ANOVA	F(5,42) = 5.39, p = 0.0006	Tukey
3A	*Kcnb1*^{G379R} Expression	One-way ANOVA	F(2,19) = 0.3806, p > 0.68	n/a
3C	K_v2.1-G379R Expression	One-way ANOVA	F(2,15) = 139.9, p < 0.0001	Tukey
3E	*Kcnb1*^{fs} Expression	One-way ANOVA	F(2,22) = 11.48, p = 0.0004	Tukey
3G	K_v2.1-fs Expression	One-way ANOVA	F(2,13) = 68.6, p < 0.0001	Tukey
4E	K_v2.2 Expression	One-way ANOVA	F(2,18) = 9.525, p = 0.0015	Tukey
4G	AMIGO-1 Expression	One-way ANOVA	F(2,18) = 7.168, p = 0.0051	Tukey
5A	G379R GTCS Flurothyl	Kruskal-Wallis	H(2) = 38.92, p < 0.0001	Dunn's
5A	fs GTCS Flurothyl	One-way ANOVA	F(2,57) = 0.8234, p = 0.4441	Tukey
5B	G379R Myoclonic Jerk Flurothyl	Kruskal-Wallis	H(2) = 2.556, p = 0.2786	Dunn's
5B	G379R Time for Seizure Progression	Kruskal-Wallis	H(2) = 12.02, p = 0.0025	Dunn's
5B	fs Myoclonic Jerk Flurothyl	One-way ANOVA	F(2,50) = 2.583, p = 0.0856	Tukey
5B	fs Time for Seizure Progression	Kruskal-Wallis	H(2) = 0.2239, p = 0.8941	Dunn's
5C	6 Hz Seizure Induction	Log-Probit	p < 0.0001	n/a
5D	Seizure Incidence, WT vs. *Kcnb1*$^{R/R}$	Fisher's Exact	p < 0.001	n/a
8A	Neurological exam	One-way ANOVA	F(3,114) = 25.82, p < 0.0001	Tukey
8B	Open Field Assay-Distance	One-way ANOVA	F(3,100) = 28.31, p < 0.0001	Tukey
8C	Open Field Assay-Center Time	One-way ANOVA	F(3,102) = 8.435, p < 0.0001	Tukey
8D	Zero Maze- Open Arm Time	One-way ANOVA	F(3,97) = 35.51, p < 0.0001	Tukey
8E	Zero Maze-Distance	One-way ANOVA	F(3,96) = 19.96, p < 0.0001	Tukey
8F	Cliff Avoidance WT vs. *Kcnb1*$^{R/+}$	LogRank Mantel-Cox	p = 0.0088	n/a
8F	Cliff Avoidance WT vs. *Kcnb1*$^{R/R}$	LogRank Mantel-Cox	p < 0.0001	n/a
8F	Cliff Avoidance *Kcnb1*$^{R/+}$ vs. *Kcnb1*$^{R/R}$	LogRank Mantel-Cox	p = 0.0052	n/a
8F	Cliff Avoidance*Kcnb1*$^{fs/+}$ vs. *Kcnb1*^{WT}	LogRank Mantel-Cox	p = 0.7263	n/a
8F	Cliff Avoidance *Kcnb1*$^{fs/+}$ vs. *Kcnb1*$^{R/+}$	LogRank Mantel-Cox	p = 0.0719	n/a
8F	Cliff Avoidance *Kcnb1*$^{fs/+}$ vs. *Kcnb1*$^{R/R}$	LogRank Mantel-Cox	p = 0.0006	n/a
8G	Marble Burying	Two-way repeated measures ANOVA	F(2,41) = 3.518, p = 0.0389	Sidak